Computational Geosciences (2021) 25:1083–1104
https://doi.org/10.1007/s10596-021-10042-5

ORIGINAL PAPER

Forward modelling of geophysical electromagnetic data on unstructured grids using an adaptive mimetic finite-difference method

Hormoz Jahandari[1] · **Alex Bihlo**[1]

Received: 29 May 2020 / Accepted: 2 February 2021 / Published online: 22 March 2021

Abstract

While the mimetic finite-difference method shares many similarities with the finite-element and finite-volume methods, it has the advantage of naturally accommodating grids with arbitrary polyhedral elements. In this study, we use this attribute to develop an adaptive scheme for the solution of the geophysical electromagnetic modelling problem on unstructured grids. Starting with an initial tetrahedral grid, our mesh adaptivity implements an iterative *h*-refinement where a residual- and jump-based goal-oriented error estimator is used to mark a certain portion of the elements. The marked elements are decomposed into new tetrahedra by regular subdivision, creating an octree-like unstructured grid. Since arbitrary polyhedra are naturally permitted in the mimetic finite-difference method, the added nodes are not regarded as hanging nodes and hence any level of non-conformity can be implemented without a modification to the mimetic scheme. In this study, we consider 2-irregularity where two levels of non-conformity between the adjacent elements is permitted. We use a total field approach where the electric field is defined at the edges of the polyhedral elements and the electromagnetic source may have an arbitrary shape and location. The accuracy of the mimetic scheme and the effectiveness of the proposed mesh adaptivity are verified using benchmark and realistic examples that represent various magnetotelluric and controlled-source survey scenarios. The mesh adaptivity generates grids with refinement generally concentrated at the transmitter and receiver locations and the interfaces of materials with contrasting conductivities, and the mimetic finite-difference solutions have good agreement with the reference numerical and real data. We also demonstrate the practicality of our method using an example with an analytical solution and comparison with a standard mesh regeneration technique. The results show that our mesh adaptivity procedure can result in a higher accuracy, with similar numbers of elements, when compared with the mesh regeneration approach. Also, using a generic sparse direct solver, our method is found to be more efficient than the mesh regeneration approach in terms of computation time and memory usage. Moreover, a comparison between 1- and 2-irregularity shows the higher efficiency of the latter in terms of the number of elements required to reach a certain level of accuracy.

Keywords Unstructured mesh · Mimetic finite-difference · Electromagnetic · Mesh adaptivity

The Fortran program used for the modelling of magnetotelluric data is available upon request by sending an email to h.jahandari@mun.ca

✉ Hormoz Jahandari
h.jahandari@mun.ca

Alex Bihlo
abihlo@mun.ca

[1] Department of Mathematics and Statistics, Memorial University of Newfoundland, St. John's, Newfoundland, Canada

1 Introduction

Numerical forward modelling is an essential component of the interpretation of geophysical electromagnetic (EM) data. While the primary application of forward modelling is to simulate predicted data due to an intermediate inversion model, in a conventional gradient-based procedure, the approximation of the sensitivities also relies on numerical forward solvers [56]. One of the numerical methods that naturally accommodates the incorporation of arbitrary geological structures, such as topography, bathymetry

and the interfaces of geological layers, is the mimetic finite-difference (MFD) method. This method allows the application of grids with arbitrary elements which can be non-convex, non-conforming and with non-planar facets [111]. In this regard, the MFD method is more flexible than the conventional finite-element (FE) and finite-volume (FV) schemes and it is more akin to the mixed FE and hybrid FV methods [63, 65, 111]. In this study, we use the MFD method for the modelling of EM data on unstructured grids with polyhedral elements. We use this scheme to develop an automatic and iterative adaptive mesh refinement (AMR) tool based on local *h*-refinement and uniform decomposition of the tetrahedra. (In *h*-refinement, the mesh is locally refined or coarsened by adding or removing nodes.) To the best of our knowledge, this study presents the first application of the MFD method for the modelling of three-dimensional geophysical EM data on unstructured grids.

Traditionally, structured rectilinear grids are used for the modelling of EM data [10, 11, 26, 35, 51, 72, 74, 79, 84, 90, 91, 96–98, 102, 117, 119]. Structured grids are simple to generate and easy to work with, but these grids are not flexible enough to represent irregular structures. On the other hand, unstructured grids enable the realistic and efficient incorporation of irregular geological structures into the computational domain. Different methods have been used for the modelling of EM data: the finite-difference (FD) and finite-volume (FV) methods [47, 73, 79, 95], the integral-equation (IE) method [60, 103, 115], and the finite-element (FE) method [37, 38, 59, 75, 76, 78, 87]. Both the FE and FV methods support unstructured grids, but the FE method has gained more attention (see [55] for a comparison between these two methods). The standard FE method is relatively easy to implement and it is well-adapted to the conventional grids with tetrahedral or hexahedral elements. However, the standard FE method is not suited to grids with arbitrary polyhedral elements since the construction of basis functions for such elements is not trivial. The MFD method is one of the various modified FE, FV, and FD methods that support polyhedral elements (see [65] and the references therein). The standard MFD schemes can be seen as generalizations of the low-order FE schemes to general polyhedral elements. In this study, we develop an edge-based MFD scheme for the modelling of geophysical EM data, which can be seen as an extension of the low-order edge-based FE method to polyhedral elements. (For more on the underlying relation between the FE, MFD and FV methods, see, e.g., [7, 34, 104, 114].)

In this work, we follow the procedures and the notation used in [18, 20, 21, 63–65, 68, 111] to derive the MFD scheme. In an MFD discretization, the first step is to attribute the degrees of freedom to appropriate grid identities, such as the nodes, centroids or the faces of the elements. The collection of these degrees of freedom is referred to as a grid function and the linear combination of similar grid functions constitutes a linear space. The next step is to obtain the discrete form of the first-order operators, i.e., gradient, divergence and curl. The formation of the mimetic operators is based on a discrete vector and tensor calculus (DVTC) which results in discrete operators that mimick the important identities of continuum calculus and preserve the symmetry and positivity of the continuum operators, where these properties apply [65, 111]. This aids in mimicking the primary properties of the underlying physical problem, such as the conservation laws and maximum principles [6, 46]. There are primary operators, which are constructed based on Stokes theorem, and dual (or derived) operators, which are formed based on the primary operators and mimetic inner product matrices. The inner product matrices are formed based on consistency and stability conditions which guarantee the accuracy of the discretization and the convergence of the discrete solution [111]. Both the mimetic operators and inner product matrices act on the discrete grid functions which belong to linear spaces.

The MFD method has been used to solve a wide range of problems during the last two decades. The discretization of diffusion problems in mixed form are presented in [18–21, 53, 54], and convection-diffusion problems are addressed in [24, 109]. The modelling of flows in porous media is considered in [1, 67], elasticity and Stokes equations in [28, 29, 108, 110] and electromagnetic problems are treated in [17, 64]. Error estimates and post-processing techniques for the MFD method are developed in [6, 23, 107, 112], the multigrid method has been applied in [89] and higher-order mimetic discretizations are proposed in [28, 44, 45, 101, 112]. The MFD method has been used to develop the virtual-element method (VEM). The main difference between the FEM and VEM is that, in the VEM, the discrete spaces are virtual, i.e., they are not constructed explicitly [22, 27, 105]. For a comprehensive review of the MFD literature see [65, 111]. In geophysics, a variant of the MFD method, the mimetic finite-volume (MFV) method is used for the modelling of time-harmonic [49] and time-domain [70] geophysical EM data on rectilinear grids, and the VEM is used for the simulation of time-harmonic wave propagation [88]. In this work, we extend the application of the MFD method to the modelling of geophysical EM data on unstructured grids.

Adaptive mesh refinement has a crucial role in the efficiency of the numerical solution of forward modelling problems. The numerical domains often contain different materials with contrasting physical properties, which leads to PDE models with highly discontinuous coefficients. There are often isolated sources that are contained inside the domain. These sources are commonly represented by singular source terms leading to large variations in the

solutions. In an adaptive mesh refinement, if we intend to improve the numerical solution equally over the domain, it is typical to consider global error estimates, which give proportional measures of accuracy over the entire domain. In geophysical modelling problems, however, high accuracy is only required at limited observation locations. In this case, local, or goal-oriented, error estimates are preferred which are typically formed by weighting the global error estimate by a function that is derived by the solution of a dual (or adjoint) form of the original PDE [80, 86].

Goal-oriented *h*- and *hp*-refinement techniques have been successfully used in geophysics. (*p*-refinement is considered in a FE context, where the order of the polynomial space is adjusted to improve the solution accuracy.) The goal-oriented dual error estimate weighting (DEW) method is employed for the 2D magnetotelluric (MT) problem [58, 62] and the 2.5D controlled-source EM (CSEM) problem [61]. An alternative dual weighted residual (DWR) method [82] is applied for 2D MT and 2.5D CSEM problems [57]. For the 3D CSEM problem, an adaptive higher order FE method is studied in [93], and the goal-oriented method proposed in [80] is applied for the 3D MT problem in [71, 87]. Goal-oriented *hp*-refinement is employed for 3D MT and 2D well-logging problems in [42] and [83], respectively. In this work, we use goal-oriented error estimates within an automatic AMR procedure for the 3D modelling of MT and CSEM data. We start the AMR procedure with a coarse initial tetrahedral mesh, and then, at the end of each iteration, we use an equilibration method to mark the elements for refinement.

There are various approaches to optimize an unstructured triangular or tetrahedral grid based on the marked elements. In geophysics, it is common to use a mesh regeneration method where, typically, an external software is used to generate a completely new, often Delaunay, mesh based on the marked elements [57, 58, 61, 62, 71, 87, 93]. In this method, the elements are always triangular or tetrahedral, in 2D and 3D, respectively, which simplifies the discretization of the problem on the the regenerated grids. However, in this method, the marked elements are merely used to indicate the regions that require higher refinement and these elements are not directly refined. Also, a Delaunay method often generates extra elements to satisfy certain mesh quality criteria (often measured in terms of the highest radius-edge ratio or the minimum dihedral angle present in the mesh [94]). Therefore, a mesh regeneration procedure could potentially create more elements than necessary to improve the solution accuracy in the marked regions. Additionally, in a 3D mesh regeneration scenario, if the model contains complex internal structures and interfaces, the external Delaunay software could face convergence issues, or fail to satisfy high mesh quality, particularly, in proximity to the complex internal interfaces.

An alternative method to refine an unstructured triangular or tetrahedral mesh is the direct subdivision of the marked elements. However, this refinement could result in the addition of nodes to the edges of the elements that neighbor the marked elements which could create non-conformity between the elements, in an FE sense. The common method to avoid the creation of these additional nodes, commonly known as hanging nodes, is to also subdivide the neighboring elements. The most popular approach is the so-called red-blue refinement where the marked elements are refined by regular subdivision while their neighboring elements are refined by irregular subdivision [113]. This method preserves the conformity of the elements which, in turn, simplifies the discretization of the problem on the refined grids. Also, this refinement method is relatively simple and does not require external software. However, the irregular refinement of the neighboring elements often results in elements with lower qualities which could degrade the overall quality of the mesh. In an iterative *h*-refinement setting, a repeated irregular subdivision of the elements in a particular region could highly affect the accuracy of the solution in that region. To avoid this, the irregularly subdivided elements require derefinement, or coarsening, in the subsequent iterations, which could highly complicate the mesh refinement algorithm. Also, note that the refinement of the neighboring elements increases the number of elements without necessarily improving the accuracy of the numerical solution. The refinement of the neighboring elements can be avoided by incorporating the hanging nodes.

Compared to the FE method, the FV method can more easily accommodate hanging nodes. However, the FV method is mainly used for rectilinear grids. In the FE method, the hanging nodes may result in the discontinuity of the solution. To avoid this, a multilevel approach [8, 118] or, more often, modified basis functions are considered [39]. In the latter approach, it is possible to assign degrees of freedom to the hanging nodes [12, 25, 43, 77], or not (often referred to as constrained approximation) [2–4, 9, 32, 33, 99]. Similar to the FV method, the MFD method treats the hanging nodes as regular nodes, hence no modification of the scheme is required. However, the MFD method has the advantage that it can be more readily applied to arbitrary elements. Here, for simplicity, we do not consider any mesh-coarsening in our *h*-refinements. Also, we satisfy the so-called 2-irregularity condition where the highest level of non-conformity between the adjacent elements is two. We note, however, that the MFD method is not restricted to any level of irregularity and our scheme can be easily extended to higher levels. To evaluate the efficiency of the proposed AMR scheme based on the MFD method and regular refinement, in Section 4, we present a comparison between this method and a standard mesh regeneration technique.

The remainder of this article is organized as follows. In Section 2, first, the governing equation of the EM problem is introduced, then, the MFD concepts and formulas are described, and finally, a mimetic discretization of the governing equation is obtained. In Section 3, a goal-oriented error estimator and an AMR algorithm for the MFD scheme are proposed. This AMR procedure is verified, in Section 4, by applying to the forward modelling of MT and CSEM data and evaluated by comparison with a mesh regeneration approach, using benchmark and realistic models. Conclusions are presented in Section 5.

2 Theory

In this section, we first introduce the boundary value problem (BVP) for the geophysical EM problem. Then, we briefly describe the MFD method and, finally, discretize the presented BVP using the MFD method. In the description of the MFD method, we make use of the notation in the book by da Veiga, Lipnikov and Manzini [111] and the related papers [18, 20, 21, 63–65, 68].

2.1 Governing equations

In low-frequency geophysical applications, the total electric and magnetic fields, $\mathbf{E}$ and $\mathbf{H}$, are related by the quasi-static version of Maxwell's equations,

$$\nabla \times \mathbf{E} = -i\,\omega\,\mu_0\,\mathbf{H} \tag{1}$$

$$\nabla \times \mathbf{H} = \sigma\,\mathbf{E} + \mathbf{J}_p, \tag{2}$$

where σ is conductivity, ω is angular frequency, i is the imaginary unit, μ_0 is the magnetic permeability of free space, $\mathbf{J}_p$ is the primary EM source and a time-dependence of $e^{i\omega t}$ is assumed. In general, σ and μ_0 are 3×3 symmetric positive-definite tensors. Taking the curl of Eq. 1 and substituting in Eq. 2 gives the Helmholtz equation for the electric field,

$$\nabla \times (i\omega\mu_0)^{-1}\nabla \times \mathbf{E} + \sigma\,\mathbf{E} = -\mathbf{J}_p. \tag{3}$$

Here, we approximate the electric source(s) geometry by n piecewise-linear segments. If we denote the position vectors of the end points of a source segment as $\mathbf{x}_a$ and $\mathbf{x}_b$, and its centre as $\mathbf{x}_m$, the source term can be characterized as

$$\mathbf{J}_p = \sum_{i=1}^{n} J_{p,\,i}\;\delta\left(\mathbf{x}-\mathbf{x}_{m,\,i}\right)\left(\mathbf{x}_{b,\,i}-\mathbf{x}_{a,\,i}\right), \tag{4}$$

where $J_{p,\,i}$ is the magnitude of the i^{th} source segment, δ is the Dirac delta function and we assume that the electric current direction is from $\mathbf{x}_{a,\,i}$ to $\mathbf{x}_{b,\,i}$. We pose the EM modelling problem by defining the computational domain and its boundary as Ω and $\partial\Omega$, respectively, and using the PDE in Eq. 3, to write the BVP as

$$\nabla \times (i\omega\mu_0)^{-1}\,\nabla \times \mathbf{E} + \sigma\,\mathbf{E} = -\mathbf{J}_p \quad \text{in } \Omega, \tag{5}$$

subject to Dirichlet boundary condition for $\mathbf{E}$, imposed on $\partial\Omega$. In the following sections, we first briefly introduce the MFD method and then derive an edge-based discretization of the BVP given by Eq. 5.

2.2 The MFD method

As mentioned in the introduction, the basis of mimetic discretization of a BVP is to replace the first-order continuum operators of the corresponding PDE with discrete operators that satisfy the principal identities of continuum calculus. There are two kinds of mimetic operators: primary operators, which are constructed based on Stokes theorem, and dual (or derived) operators, which are formed by the support of the primary operators and the aid of mimetic inner product matrices. In the following, we describe the mimetic inner product matrices and mimetic operators that are required for the mimetic discretization given in Section 2.3.

2.2.1 Mimetic inner product matrices

Let u and v be two arbitrary fields defined on a bounded domain $\Omega \in \mathbb{R}^3$, and let Ω_h be a partition of Ω into polyhedra. We denote the discrete analog of u and v over Ω_h by u_h and v_h, respectively, where $u_h, v_h \in \mathscr{S}_h$, and $\mathscr{S}_h$ is a discrete space over Ω_h. $\mathscr{S}_h$ represents the space of face or edge functions, designated here by $\mathscr{F}_h$ and $\mathscr{E}_h$, respectively. The inner product of u_h and v_h over Ω_h is a sum over the local inner products,

$$[\,u_h,\,v_h\,]_{\mathscr{S}_h} = \sum_{\mathsf{P}\in\,\Omega_h} \left[\,u_{h,\mathsf{P}},\,v_{h,\mathsf{P}}\,\right]_{\mathscr{S}_h,\mathsf{P}} \qquad \forall\, u_h, v_h \in \mathscr{S}_h, \tag{6}$$

where P is a polyhedral element of Ω_h and $u_{h,\mathsf{P}}$ and $v_{h,\mathsf{P}}$ are the restrictions of u_h and v_h to P, respectively. The local inner products should satisfy the consistency condition

$$\left[\,u_{h,\mathsf{P}},\,v_{h,\mathsf{P}}\,\right]_{\mathscr{S}_h,\mathsf{P}} = \int_{\mathsf{P}} R^{\mathscr{S}}_{\mathsf{P}}\left(u_{h,\mathsf{P}}\right)\,R^{\mathscr{S}}_{\mathsf{P}}\left(v_{h,\mathsf{P}}\right)\,dV, \tag{7}$$

where $R^{\mathscr{S}}_{\mathsf{P}}$ is a reconstruction operator that maps the discrete grid functions, $u_{h,\mathsf{P}}$ and $v_{h,\mathsf{P}}$, into continuum functions, over P. For elements with simple geometry, e.g., tetrahedra or hexahedra, $R^{\mathscr{S}}_{\mathsf{P}}$ can be easily built using appropriate basis functions. However, for general polyhedral elements this is not a trivial task. In the MFD method, the inner products are constructed with the aid of

inner product matrices. The local inner products introduced in Eq. 6 are represented as

$$\left[u_{h,\mathsf{P}}, v_{h,\mathsf{P}} \right]_{\mathscr{S}_h,\mathsf{P}} = u_{h,\mathsf{P}}^T \, \mathsf{M}_{\mathscr{S}_h,\mathsf{P}} \, v_{h,\mathsf{P}} \qquad \forall u_{h,\mathsf{P}}, v_{h,\mathsf{P}}, \tag{8}$$

where $\mathsf{M}_{\mathscr{S}_h,\mathsf{P}}$ is a local inner product matrix for the linear space $\mathscr{S}_h$. $\mathsf{M}_{\mathscr{S}_h,\mathsf{P}}$ is $m \times m$, where m is the number of degrees of freedom in $\mathscr{S}_h$, for P [69, 104, 111]. To ensure the accuracy of an MFD scheme and the convergence of its solution, $\mathsf{M}_{\mathscr{S}_h,\mathsf{P}}$ should be calculated such that it satisfies the consistency condition given by Eq. 7, and stability conditions. It is shown that this is achieved by defining this matrix such that

$$\mathsf{M}_{\mathscr{S}_h,\mathsf{P}} \, \mathsf{N}_{\mathscr{S}_h,\mathsf{P}} = \mathsf{R}_{\mathscr{S}_h,\mathsf{P}}, \tag{9}$$

where $\mathsf{N}_{\mathscr{S}_h,\mathsf{P}}$ and $\mathsf{R}_{\mathscr{S}_h,\mathsf{P}}$ are rectangular matrices [64, 111]. Knowing these matrices, a possible formula to calculate the local inner product matrix is

$$\mathsf{M} = \mathsf{M}^0 + \mathsf{M}^1 = \mathsf{R} \left(\mathsf{R}^T \mathsf{N} \right)^{-1} \mathsf{R}^T + \frac{1}{m} \operatorname{tr} \left(\mathsf{M}^0 \right) \left(\mathsf{I} - \mathsf{N} \left(\mathsf{N}^T \mathsf{N} \right)^{-1} \mathsf{N}^T \right), \tag{10}$$

where the subscripts are dropped for convenience. Analytical expressions for calculating the local N and R matrices, for the linear spaces $\mathscr{F}_h$ and $\mathscr{E}_h$, are given in [111]. Having calculated the local M matrices, the global inner product matrices are constructed using assembly processes similar to those used in the standard FE methods.

2.2.2 Mimetic operators

The primary mimetic operators are constructed based on Stokes theorem. The discrete primary curl operator, curl_h, acts from $\mathscr{E}_h$ to $\mathscr{F}_h$ ($\text{curl}_h : \mathscr{E}_h \to \mathscr{F}_h$). Let $\partial\mathsf{f}$ represent the boundary of face f, and τ_f the unit tangential vector along this boundary. τ_f has a counter-clockwise direction when observed from the end of the unit normal vector of f, $\mathbf{n}_\mathsf{f}$. The discrete primary curl operator is derived based on Stokes theorem applied to face f,

$$\int_\mathsf{f} (\text{curl}\, \mathbf{E}) \cdot \mathbf{n}_\mathsf{f} \, dS = \int_{\partial\mathsf{f}} \mathbf{E} \cdot \tau_\mathsf{f} \, dL. \tag{11}$$

Here, we consider an edge-based method where the discrete values of $\mathbf{E}$ are defined at the edges, i.e., $\mathbf{E}_h \in \mathscr{E}_h$. We denote the edges that form $\partial\mathsf{f}$ by $\mathsf{e} \in \mathscr{E}_\mathsf{f}$, and we let E_e represent the value of $\mathbf{E}_h$ associated with e. Then, using (11), the discrete curl operator, applied to face f, is defined as

$$(\text{curl}_h \, \mathbf{E}_h)_\mathsf{f} = \frac{1}{|\mathsf{f}|} \sum_{\mathsf{e} \in \mathscr{E}_\mathsf{f}} \alpha_{\mathsf{f},\mathsf{e}} \, |\mathsf{e}| \; E_\mathsf{e}, \tag{12}$$

where $|\mathsf{e}|$ and $|\mathsf{f}|$ are the length of e and the area of f, respectively. $\alpha_{\mathsf{f},\mathsf{e}} = \pm 1$ signifies the mutual orientation of $\mathbf{n}_\mathsf{f}$ and $\tau_{\mathsf{f},\mathsf{e}}$, where $\tau_{\mathsf{f},\mathsf{e}}$ is the unit tangential vector along e. We note that $\mathbf{n}_\mathsf{f}$ and e have fixed orientations.

The dual mimetic operators are derived based on Green's formulas. We derive the discrete mimetic dual curl operator, $\widetilde{\text{curl}}_h$ ($\widetilde{\text{curl}}_h : \mathscr{F}_h \to \mathscr{E}_h$), following the procedure in [111]. Consider the electric and magnetic fields, $\mathbf{E}$ and $\mathbf{H}$, defined on Ω. Green's formula for the curl operator, with proper boundary conditions, indicates

$$\int_\Omega \mathbf{H} \cdot \; \text{curl}\; \mathbf{E} \; dV = \int_\Omega (\text{curl}\; \mathbf{H}) \cdot \mathbf{E} \; dV. \tag{13}$$

If $\mathbf{E}_h$ and $\mathbf{H}_h$ are edge and face functions, then (6), (7) and (13) suggest

$$[\text{curl}, \; \mathbf{E}_h, \mathbf{H}_h]_{\mathscr{F}_h} \equiv \left[\mathbf{E}_h, \widetilde{\text{curl}}_h \, \mathbf{H}_h \right]_{\mathscr{E}_h} \qquad \forall \; \mathbf{E}_h \in \mathscr{E}_h, \mathbf{H}_h \in \mathscr{F}_h. \tag{14}$$

The discrete Green's formula in Eq. 14 can be approximated using the global inner product matrices for the spaces of edge and face functions, $\mathsf{M}_{\mathscr{E}_h}$ and $\mathsf{M}_{\mathscr{F}_h}$, respectively. Using relations (6) and (8), we can rewrite (14) as

$$\mathbf{E}_h^T \, \text{curl}_h^T \, \mathsf{M}_{\mathscr{F}_h} \, \mathbf{H}_h \equiv \mathbf{E}_h^T \mathsf{M}_{\mathscr{E}_h} \, \widetilde{\text{curl}}_h \; \mathbf{H}_h. \tag{15}$$

Since $\mathbf{H}_h$ and $\mathbf{E}_h$ are arbitrary functions, we derive the dual curl operator as

$$\widetilde{\text{curl}}_h \equiv \mathsf{M}_{\mathscr{E}_h}^{-1} \, \text{curl}_h^T \, \mathsf{M}_{\mathscr{F}_h}. \tag{16}$$

In the next section, we use the primary and dual curl operators, given by Eqs. 12 and 16, to derive a mimetic discretization of the EM problem.

2.3 Mimetic discretization of the EM problem

In this section, we derive a discretization of the BVP given by Eq. 5 using the MFD methodology described in Section 2.2. For an edge-based discretization, where the discrete electric field $\mathbf{E}_h$ is defined at the edges of Ω_h, we use the primary and dual mimetic operators, curl_h and $\widetilde{\text{curl}}_h$, and $\mathbf{E}_h \in \mathscr{E}_h$, to discretize (5) as

$$\widetilde{\text{curl}}_h \; (i\omega\mu_0)^{-1} \; \text{curl}_h \, \mathbf{E}_h + \sigma \, \mathbf{E}_h = -\Pi^{\mathscr{E}} \left(\mathbf{J}_p \right), \tag{17}$$

or

$$\widetilde{\text{curl}}_h \; \mu_0^{-1} \; \text{curl}_h \, \mathbf{E}_h + i\omega\sigma \, \mathbf{E}_h = -i\omega \, \Pi^{\mathscr{E}} \left(\mathbf{J}_p \right), \tag{18}$$

where $\Pi^{\mathscr{E}}(\cdot)$ is a global projection operator that projects the given function onto $\mathscr{E}_h$. Also, $\Pi^{\mathscr{E}}(\cdot) = \sum_{\mathsf{P} \in \Omega_h} \Pi_\mathsf{P}^{\mathscr{E}}(\cdot)$, where $\Pi_\mathsf{P}^{\mathscr{E}}(\cdot)$ is a local projection operator which will be defined later. We can use (16) to rewrite (18) as

$$\left[\text{curl}_h^T \, \mathsf{M}_{\mathscr{F}_h} \, \mu_0^{-1} \, \text{curl}_h + i\omega \, \mathsf{M}_{\mathscr{E}_h} \sigma \right] \mathbf{E}_h = -i\omega \; \mathsf{M}_{\mathscr{E}_h} \, \Pi^{\mathscr{E}} \left(\mathbf{J}_p \right). \tag{19}$$

In this relation, to correctly implement σ and μ_0, which are in general in the form of tensors, we need to weight the global inner product matrices $\mathsf{M}_{\mathscr{E}_h}$ and $\mathsf{M}_{\mathscr{F}_h}$, by σ and μ_0^{-1}, respectively. To do this, the corresponding local inner product matrices, $\mathsf{M}_{\mathscr{E}_h,\mathsf{P}}$ and $\mathsf{M}_{\mathscr{F}_h,\mathsf{P}}$, defined by Eq. 10, should be weighted by σ and μ_0^{-1} tensors for element P. We denote the resulting weighted global inner product matrices as $\mathsf{M}_{\mathscr{E}_h,\sigma}$ and $\mathsf{M}_{\mathscr{F}_h,\mu}$.

We also need to correctly calculate $\mathsf{M}_{\mathscr{E}_h}\,\Pi^{\mathscr{E}}\left(\mathbf{J}_p\right)$, on the right-hand side of Eq. 19. In Eq. 4, we defined $\mathbf{J}_p$ as an arbitrary electric source with a piecewise linear geometry. We denote the section of $\mathbf{J}_p$ that is located inside element P by $\mathbf{J}_{p,\mathsf{P}}$. We also consider the linear edge-based interpolation functions $\mathbf{N}_{\mathsf{e},\mathsf{P}}$, $\mathsf{e}\in\mathscr{E}_\mathsf{P}$, where $\mathscr{E}_\mathsf{P}$ is the set of edges of P. A property of $\mathbf{N}_{\mathsf{e},\mathsf{P}}$ is that it has a unit value at e and zero at the other edges of P. Therefore, we can write the right-hand side of Eq. 19 as

$$\mathsf{M}_{\mathscr{E}_h}\;\Pi^{\mathscr{E}}\left(\mathbf{J}_p\right)\;=\;\sum_{\mathsf{P}\in\,\Omega_h}\Pi^{\mathscr{E}}_{\mathsf{P}}\left(\mathbf{N}_{\mathsf{e},\mathsf{P}}\right)\;\mathsf{M}_{\mathscr{E}_h,\mathsf{P}}\;\Pi^{\mathscr{E}}_{\mathsf{P}}\left(\mathbf{J}_{p,\mathsf{P}}\right).\quad(20)$$

Using (7) and (8), (20) can be rewritten as

$$\mathsf{M}_{\mathscr{E}_h}\;\Pi^{\mathscr{E}}\left(\mathbf{J}_p\right)\;=\;\sum_{\mathsf{P}\in\,\Omega_h}\int_{\mathsf{P}}\mathbf{N}_{\mathsf{e},\mathsf{P}}\cdot\mathbf{J}_{p,\mathsf{P}}\;dV.\quad(21)$$

Since calculating $\mathbf{N}_{\mathsf{e},\mathsf{P}}$ for the general polyhedron P is not trivial, we define $\Pi^{\mathscr{E}}_{\mathsf{P}}(\cdot)$ such that it projects the given function, here $\mathbf{J}_{p,\mathsf{P}}$, to those edges of P that align with the six edges of an equivalent tetrahedron. We refer to this equivalent tetrahedron and the corresponding edge-based interpolation functions as $\tilde{\mathsf{P}}$ and $\mathbf{N}_{\tilde{\mathsf{P}}}$, respectively, and we denote the set of edges of P that align with the edges of $\tilde{\mathsf{P}}$ as $\bar{\mathscr{E}}_\mathsf{P}$. Therefore, we can define $\mathbf{N}_{\mathsf{e},\mathsf{P}}$ in Eq. 21 such that $\mathbf{N}_{\mathsf{e},\mathsf{P}}=\left(|\mathsf{e}|/|\tilde{\mathsf{e}}|\right)\,\mathbf{N}_{\tilde{\mathsf{e}},\tilde{\mathsf{P}}}$, if $\mathsf{e}\in\bar{\mathscr{E}}_\mathsf{P}$ and e aligns with edge $\tilde{\mathsf{e}}$ of $\tilde{\mathsf{P}}$, and $\mathbf{N}_{\mathsf{e},\mathsf{P}}=0$, if $\mathsf{e}\notin\bar{\mathscr{E}}_\mathsf{P}$.

Using (19) and the newly defined weighted inner product matrices, $\mathsf{M}_{\mathscr{E}_h,\sigma}$ and $\mathsf{M}_{\mathscr{F}_h,\mu}$, the mimetic discretization of the EM problem in Eq. 5 reads: Find $\mathbf{E}_h\in\mathscr{E}_h$ such that

$$\left[\,\mathrm{curl}_h^T\,\mathsf{M}_{\mathscr{F}_h,\mu}\;\mathrm{curl}_h+i\,\omega\,\mathsf{M}_{\mathscr{E}_h,\sigma}\right]\mathbf{E}_h=-i\omega\;\mathsf{M}_{\mathscr{E}_h}\,\Pi^{\mathscr{E}}\left(\mathbf{J}_p\right),\quad(22)$$

along with Dirichlet boundary conditions for $\mathbf{E}_h$, imposed on $\partial\Omega$, and the right-hand side given by Eq. 21. This scheme can be seen as a generalization of the lowest-order edge-based FE method to polyhedral elements [46, 111]. In Section 4, we employ the mimetic discretization in Eq. 22 to solve EM problems using a goal-oriented AMR scheme. The goal-oriented error estimator and the details of mesh adaptivity are described in Section 3.

3 Goal-oriented mesh adaptivity

In this section, we first introduce a goal-oriented error estimator for the edge-based MFD scheme derived in Section 2.3, and then describe our mesh adaptivity based on this error estimator. We will use this goal-oriented mesh adaptivity in Section 4, to solve various examples of the geophysical EM problem.

3.1 Goal-oriented error estimator

We consider a standard FE-type error estimator that is based on the discontinuity of the normal component of current density, $\mathbf{J}_h=\sigma\,\mathbf{E}_h$, at the faces of the elements, and a residual-based term. The piecewise-constant global error estimator η_h is written as

$$\eta_h^2=\sum_{\mathsf{P}\in\,\Omega_h}\eta_{h,\mathsf{P}}^2,\quad(23)$$

where $\eta_{h,\mathsf{P}}$ is the error estimator for element P, and it consists of residual- and jump-based terms,

$$\eta_{h,\mathsf{P}}^2\;\equiv\;h_\mathsf{P}^2\,\|\,\mathbf{r}\,\|_{2,\,\mathsf{P}}^2+\frac{1}{2}\sum_{\mathsf{f}\in\partial\mathsf{P}}\left(\;h_\mathsf{f}^2\;[\![\,\mathbf{J}_h\,]\!]_\mathsf{f}\;\right)^2.\quad(24)$$

In this expression, $[\![\,\mathbf{J}_h\,]\!]_\mathsf{f}$ represents the jump of the normal component of $\mathbf{J}_h$ on face f of element P, h_P and h_f denote the diameters of P and f, respectively, and $\mathbf{r}$ is the residual of Eq. 5 [14]. We note that the calculation of $\eta_{h,\mathsf{P}}$ in Eq. 24, in an FE sense, requires the knowledge of edge-based interpolation functions of P. Since the calculation of these functions for a polyhedral P is not trivial, we approximate $\eta_{h,\mathsf{P}}$ by $\eta_{h,\tilde{\mathsf{P}}}$, where $\tilde{\mathsf{P}}$ is a tetrahedron that is equivalent to P. The solution at edge $\tilde{\mathsf{e}}$ of $\tilde{\mathsf{P}}$ is calculated as a weighted average of the solutions at those edges of P that align with $\tilde{\mathsf{e}}$. For this averaging, the weight for edge e of P is given by $|\mathsf{e}|/|\tilde{\mathsf{e}}|$.

While the global error estimator defined here, η_h, is intended to give a proportional measure of accuracy over the entire domain, in many applications, including geophysical forward modelling, high accuracy is only required at limited observation locations. In such applications, it is common to use a local, or goal-oriented, error estimator which is typically constructed by weighting η_h by a function which is derived by solving a dual (adjoint) form of the original PDE. In this study, we use the standard method laid out in [15, 16, 80, 86] and define our goal-oriented error estimator, η_h^g, as

$$\eta_h^g\;\equiv\;\sum_{\mathsf{P}\in\,\Omega_h}\left(\eta_{h,\mathsf{P}}\right)^a\;\left(\eta_{h,\mathsf{P}}^w\right)^b,\quad(25)$$

where η_h^w is an error estimator calculated based on the solution of an adjoint of the primary forward problem. While the standard value for a and b is unity, we found that a relatively larger value for b is often necessary to achieve

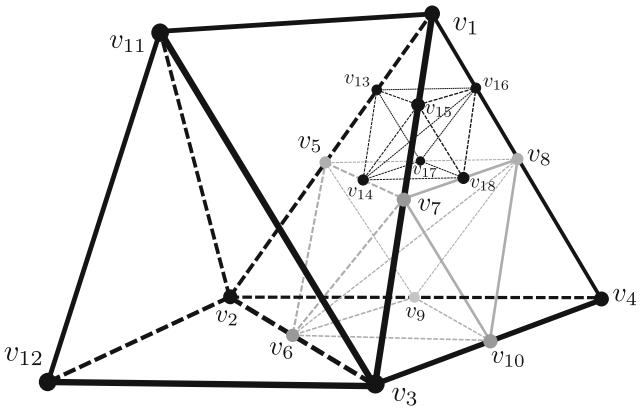

Fig. 1 An example of the regular refinement of marked elements in two consecutive iterations. In the first iteration, tetrahedron $\{v_1, v_2, v_3, v_4\}$ is subdivided into eight new tetrahedra by the addition of nodes v_5, v_6, v_7, v_8, v_9 and v_{10}. Note that this refinement increases the numbers of nodes, edges and faces of its neighbor $\{v_1, v_2, v_3, v_{11}\}$. Also, note the node, v_6, added to element $\{v_{11}, v_2, v_3, v_{12}\}$. In the second iteration, $\{v_1, v_5, v_7, v_8\}$ is subdivided into eight new tetrahedra by the addition of nodes v_{13}, v_{14}, v_{15}, v_{16}, v_{17} and v_{18}

a proper refinement at the observation locations. Based on our experiments, we chose $a = 0.5$ and $b = 1.5$, for our calculations.

The adjoint problem, required to calculate η_h^w in Eq. 25, has the same coefficient matrix as the primary problem but a different right-hand side. This modified right-hand side typically represents fictitious source terms located at the target regions [80, 87]. Here, we use electric sources located at the edges of the elements that contain the observation points. Let Ω_h^w denote the set of elements that contain the observation points. We introduce $\eta_h^* = \sum_{\mathsf{P}\in\,\Omega_h} \eta_{h,\mathsf{P}}^*$, where $\eta_{h,\mathsf{P}}^* = \eta_{h,\mathsf{P}}$, if $\mathsf{P}\in\,\Omega_h^w$ and zero otherwise. Hence, we define the adjoint problem of the edge-based MFD problem, given by Eq. 22, as finding $\mathbf{E}_h^w \in \mathscr{E}_h$ such that

$$\left[\,\mathrm{curl}_h^T\,\mathsf{M}_{\mathscr{F}_h,\,\mu}\,\mathrm{curl}_h + i\,\omega\,\mathsf{M}_{\mathscr{E}_h,\sigma}\right]\mathbf{E}_h^w = -i\omega\,\mathsf{M}_{\mathscr{E}_h}\,\Pi^{\mathscr{E}}(\eta_h^*), \tag{26}$$

subject to vanishing Dirichlet boundary conditions for $\mathbf{E}_h^w$, imposed on $\partial\Omega$. We note that the amplitude of the source term in Eq. 26 reflects the error estimator of the elements in Ω_h^w. We also note that there is an additional cost to the solution of the adjoint problem, given by Eq. 26. However, in this work, we use the sparse direct solver MUMPS [5], where the factorization of the coefficient matrices can be reused for multiple right-hand sides. Since the factorization step is the single most expensive part of a direct solution, the cost of the solution of the adjoint problem is minimal.

In Section 3.2, we describe our mesh adaptivity where the goal-oriented error estimator given by Eq. 25, η_h^g, is used to identify the elements to be refined.

3.2 Mesh generation and adaptivity

In this section, we briefly introduce our mesh adaptivity for the MFD scheme described in Section 2. In our iterative AMR approach, we use TetGen [94], which is an open-source Delaunay mesh generation program, for generating the initial grid only. From the second iteration onward, at the start of each iteration, we construct a new mesh by subdividing the elements that are marked at the end of the previous iteration. This procedure is described by Algorithm 1, which consists of a main loop that goes through all the current elements of the mesh and replaces them with new elements. If a current element is marked, then it is subdivided into eight new tetrahedra, and if not, then it is replaced with a single new element. Afterwards, the identities of the new elements, i.e., nodes, edges and faces, are formed and the connectivity between these elements and their neighboring elements, in the new mesh, are determined.

The marking of the elements is based on an equilibration strategy and the goal-oriented error estimator presented in Section 3.1. In this method, the elements over which the sum of the error estimator values is a certain fraction, β, of the total sum of error estimator values are marked [3, 113]. We also used a maximum method to assign a lower bound for the percent of the elements marked at each iteration. The maximum method is based on refining a fixed percent, γ, of the elements with the highest values of the error estimator. In this study, we used $\beta = 0.5$ and $\gamma = 10\%$.

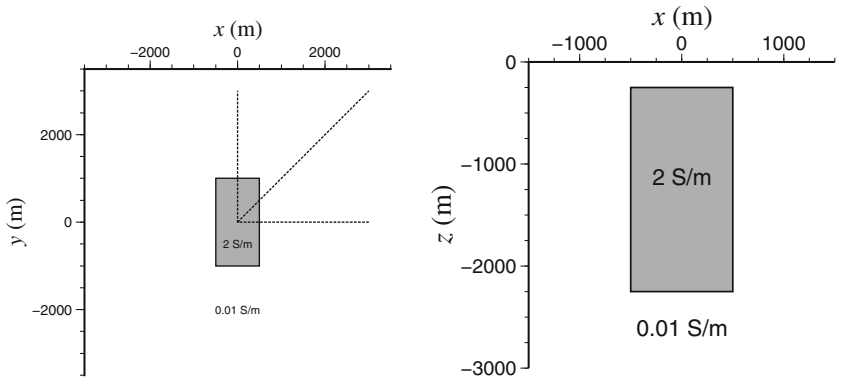

Fig. 2 The left and right panels show, respectively, the plan and side views of the 3D-1A model used in the first example. The anomalous block is shown in gray and the observation profiles are shown as dashed-lines

Algorithm 1 The procedure to refine the current mesh, Ω_h, by the regular subdivision of marked elements.

procedure Regular refinement (*cells*, *neighs*, *marked*)
▷ *cells* is the set of elements in Ω_h, *neighs* gives the neighbors of the elements in *cells*, and *marked* is the set of elements in Ω_h that are marked for refinement.
for each *cell* in *cells* **do**
if *cell* is in *marked* **then**
▷ Create eight new elements by the regular subdivision of *cell*.
▷ Set the connectivity between the eight new elements.
else
▷ Create one new element which is similar to *cell*.
end if
▷ Create new faces, edges and nodes that correspond to the new element(s).
for each *neigh* in *neighs* (*cell*) **do**
if *neigh* is already chosen as *cell* in the main (outer) loop **then**
▷ Find the face that is shared by *cell* and *neigh*.
▷ Find the sets of newly created elements *cell** and *neigh** that are attached to this face.
▷ Set the connectivity between the elements in *cell** and *neigh**.
end if
end for
end for
end procedure

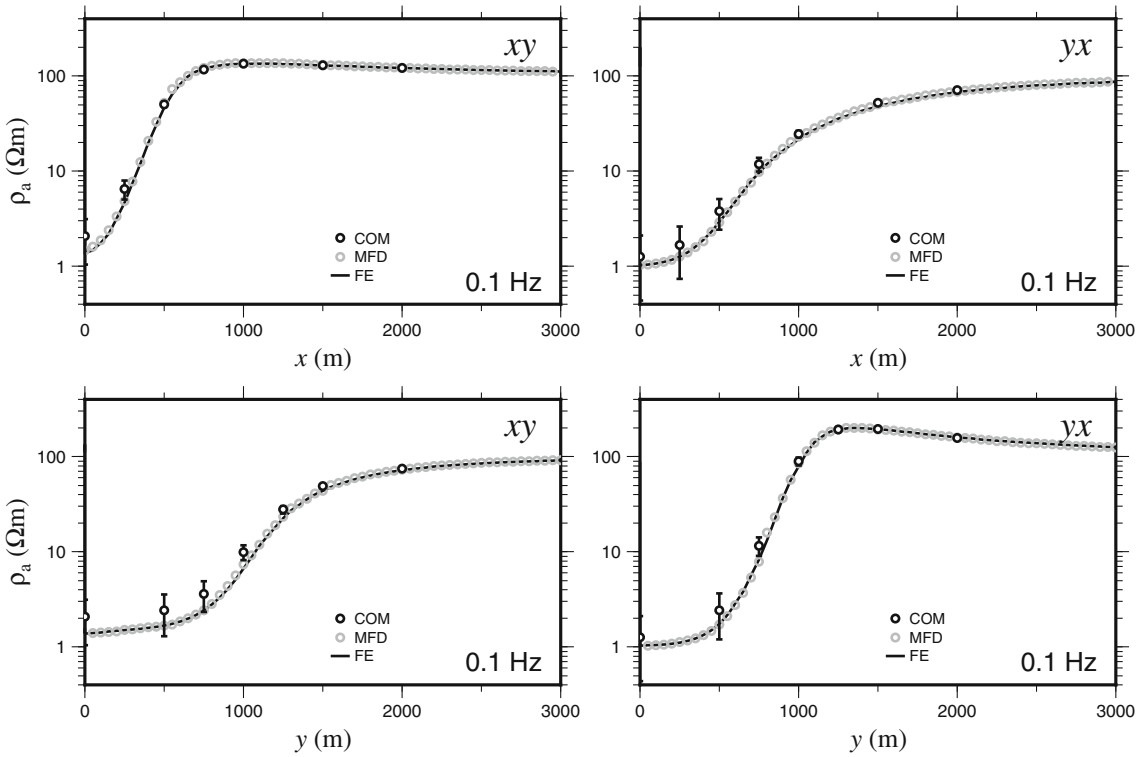

Fig. 3 The off-diagonal components of apparent resistivity, xy and yx, at the two observation profiles that are along the x and y axes, in the first example. The mimetic finite-difference (MFD) solutions are compared with reference values presented in [120] (COM) and finite-element solutions (FE). The MFD data correspond to the final grid shown in Fig. 5

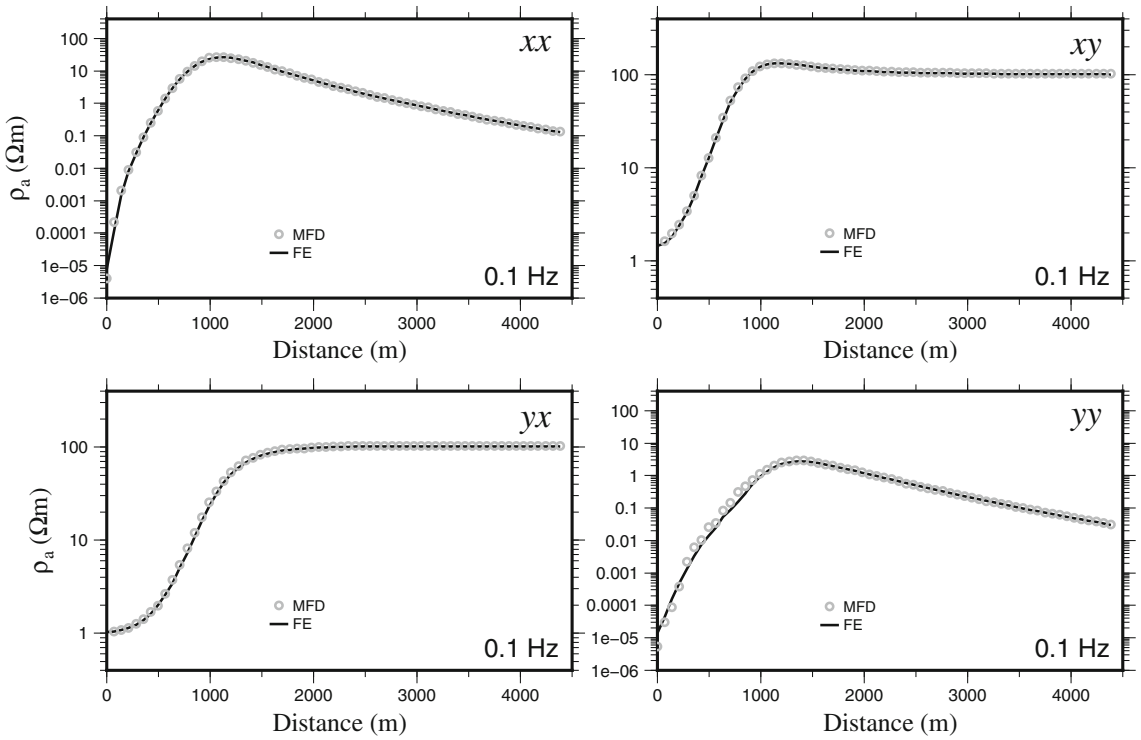

Fig. 4 The four components of apparent resistivity at the third profile (along the $x = y$, $z = 0$ line), in the first example. The mimetic finite-difference (MFD) solutions are compared with finite-element solutions (FE). The MFD data correspond to the final grid shown in Fig. 5

As a consequence of the iterative mesh refinement, starting from the second iteration, cells with different levels are present in the mesh. We assign the level of one to the cells of the initial mesh. The level of the eight elements that are created by the subdivision of cell P is equal to the level of P plus one. As depicted in Fig. 1, a marked cell is subdivided into eight new tetrahedra by regular refinement (see, e.g., [81]). Therefore, our mesh adaptivity using the MFD method can be seen as an extension of the conventional 1-irregular octree method on hexahedral grids using the FV and FE methods, as in [30, 31, 41, 42, 48, 50, 52], to unstructured tetrahedral grids and a higher level of irregularity. We also refer the reader to the mesh adaptivities using the MFD method on 2D grids with general polygonal elements, in [6, 66, 106].

When an element P is marked and refined, it potentially results in an addition of faces and nodes to those neighbors of P which are of the same cell level as P, l_{P}, or of levels lower than l_{P}. Therefore, starting from the second iteration, not all the elements in the grid are tetrahedral (see Fig. 1). As mentioned before, we allow two levels of difference in cell level between the adjacent elements. To enforce this so-called 2-irregularity [9, 85, 92, 100], when we mark element P, we also search through its neighbors and mark those neighbors of P that are of cell levels lower than $l_{\mathsf{P}} - 1$, too. We note, however, that the mimetic operators and inner product matrices described in Section 2.2, are not restricted to any specific element shape or number of facets, and therefore, an extension to a higher level of irregularity is straightforward.

4 Examples

In this section, we give five examples to verify and evaluate our mimetic finite-difference scheme and the adaptive mesh refinement approach presented in Sections 2 and 3. The first example represents a standard MT model with a plane--wave source while the second and third examples represent benchmark models in which the responses of halfspaces with anomalous blocks due to electric and magnetic sources are calculated. In all three examples, we compared the

Table 1 Computation time and memory usage, using MUMPS, and the number of elements, for the five iterations of the adaptive MFD scheme in the first (MT) example

Iteration no.	0	1	2	3	4	5
No. of elements	25558	52396	107416	220207	451431	925436
Time (s)	1	2	5	15	33	78
Memory (MB)	152	417	1139	2693	5950	13291

Iteration 0 refers to the initial model

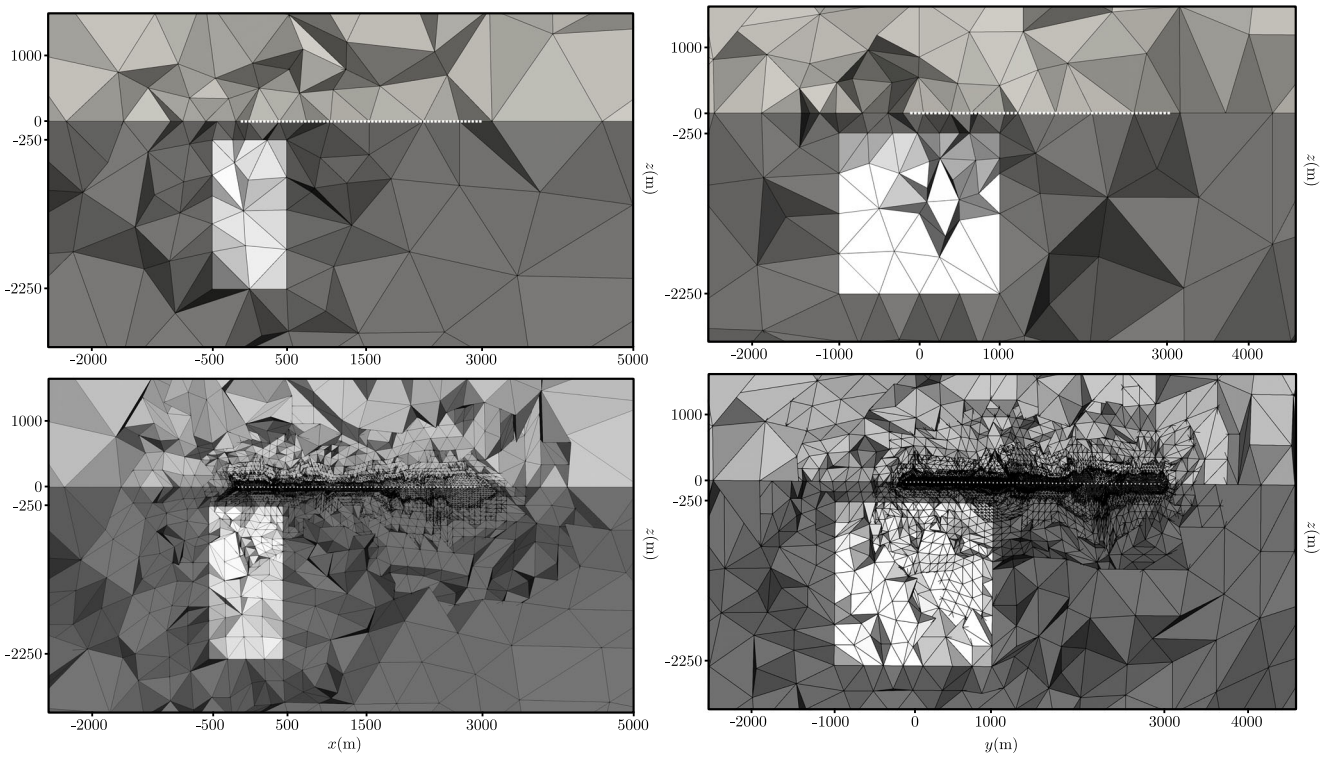

Fig. 5 Close-ups of the sections of the initial (top) and final (bottom) grids through the two observation profiles that are along the x and y axes, for goal-oriented mesh adaptivity in the first example. Light and dark gray show the air and ground regions and white shows the anomalous block. The white dots show the observation points. The final grid corresponds to the MFD data given in Figs. 3 and 4

results of the MFD scheme with solutions of an edge-based finite-element scheme, calculated for sufficiently fine tetrahedral grids. The fourth example corresponds to a real-life geological model with topography and the mimetic solutions were compared against real helicopter-borne EM (HEM) data. The fifth example comprises an infinitesimal electric dipole on a homogeneous halfspace. Analytical solutions due to this model were used to compare the results of the presented adaptive MFD scheme with

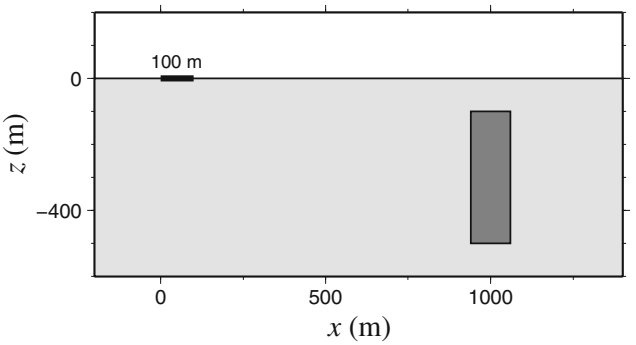

Fig. 6 A vertical section at $y = 0$ m, of the model in the second example. The thick black segment shows the location of the 100 m grounded wire source. The dark gray rectangle indicates the anomalous region

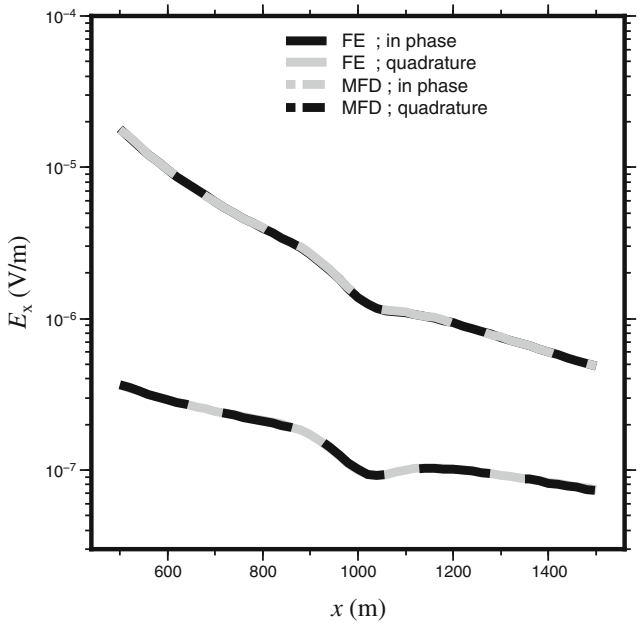

Fig. 7 The x-component of the total electric field at the observation profile for mesh adaptivity with the grounded wire source model in the second example. The final MFD results are compared with FE solutions. The MFD solutions correspond to the final grid shown in Fig. 9

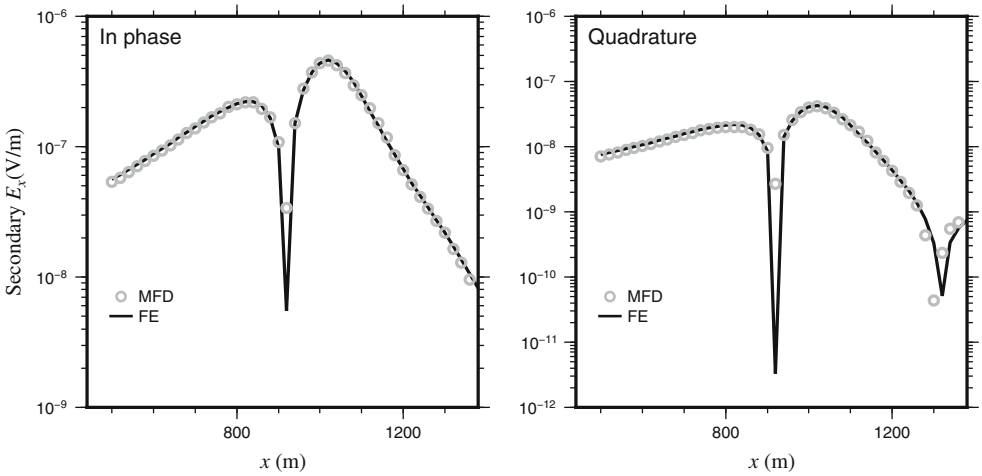

Fig. 8 The x-component of the scattered electric field at the observation profile for mesh adaptivity with the grounded wire source model in the second example. The final MFD results are compared with FE solutions. The MFD solutions correspond to the final grid shown in Fig. 9

those of a conventional mesh regeneration approach. For the controlled-source examples, we considered a vanishing Dirichlet boundary condition, and for the MT example an inhomogeneous Dirichlet boundary condition approximated by a 1D Earth model. In all the examples, we used the iterative goal-oriented mesh adaptivity described in Section 3. The MUMPS sparse direct solver (specifically, library ZMUMPS, for complex-valued matrices) [5] and TetGen [94] were used for solving the systems of equations and for generating the initial grids, respectively. For the first and fourth examples, the computation time and memory usage are reported for the adaptive MFD scheme. For

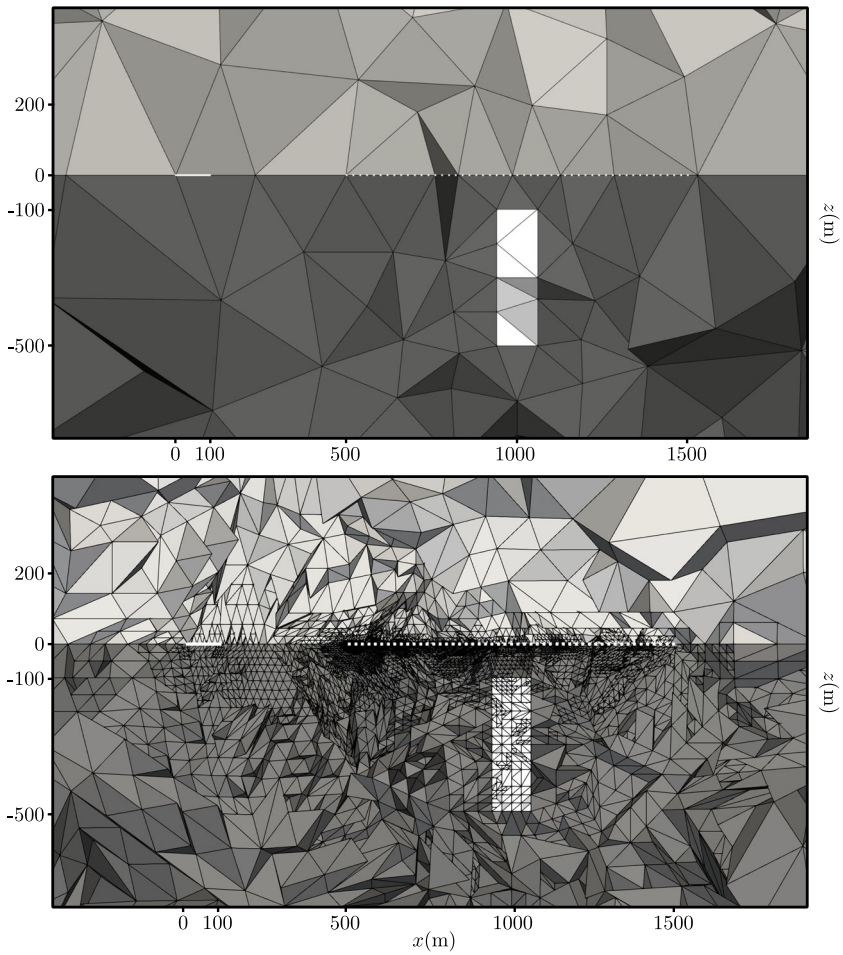

Fig. 9 Close-ups of the sections of the initial (top) and final (bottom) grids through the observation profile, along the x-axis, for goal-oriented mesh adaptivity in the second example. Light and dark gray show the air and ground regions and white shows the anomalous block. The white dots and the white segment show the observation points and the grounded wire source, respectively. The final grid corresponds to the MFD data given in Figs. 7 and 8

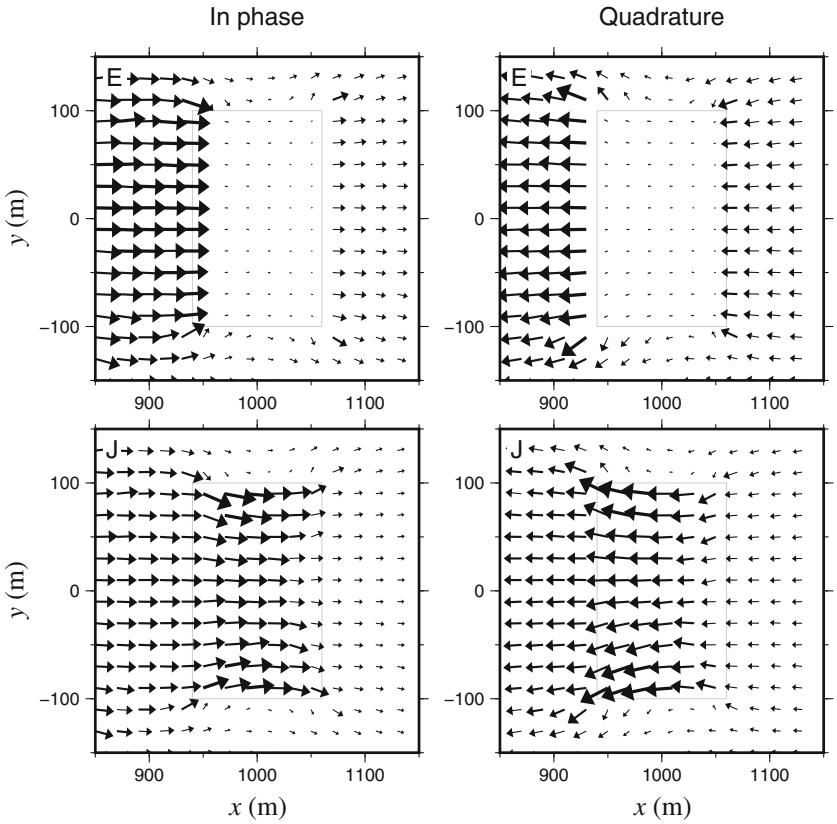

Fig. 10 The total electric field (top) and current density (bottom) for the second example, at a horizontal section at $z = -200$ m. The light gray rectangle shows the limits of the anomalous block. The sizes of the arrows are normalized by the largest arrow size in each panel

the fifth example, the resource usage is reported for both the regular refinement and mesh regeneration schemes. All the computations were performed on a Dell OptiPlex 9020 computer with a 3.60 GHz Intel Core i7-4790 CPU processor. Here, we only used a single CPU core for each modelling task, but we note that, at the cost of additional memory and CPU cores, MUMPS can be used in parallel to decrease the computation times (see, e.g., Table 1 in [56], which gives the resource usage for various numbers of cores, for solving an MT problem, using an edge-based FE scheme).

4.1 Example 1

The first example represents the COMMEMI 3D-1A model [120]. Figure 2 shows this model which comprises an anomalous block in a homogeneous halfspace. In this model, a conductive block with dimensions of $1\times2\times2$ km in the x-, y- and z-directions, respectively, is located inside a halfspace where the centre of the top of the block is at $(0, 0, -250)$ m. There were three observation profiles at the air-earth interface, along the x-axis from $(0, 0, 0)$ km to $(3, 0, 0)$ km, along the y-axis from $(0, 0, 0)$ km to $(0, 3, 0)$ km, and along the $x = y$ line, from $(0, 0, 0)$ km to $(3, 3, 0)$ km. The block and the halfspace had conductivities of 2 and 0.01 S/m, respectively. A frequency of 0.1 Hz was used. The entire computational domain had dimensions of $100\times100\times100$ km, and the initial grid had 25558 tetrahedral elements. There were 61 observation points along each observation profile. For mesh adaptivity, we used the goal-oriented error estimator described in Section 3.1 and the procedure in Section 3.2. Five iterations were used which resulted in a grid with 925436 elements.

Figure 3 shows apparent resistivity for the off-diagonal components of the impedance tensor, xy and yx, at the two profiles that are parallel to the x and y axes (the diagonal elements are zero). Figure 4 shows apparent resistivity for all components of the impedance tensor at the third profile. These figures compare the adaptive MFD results against FE

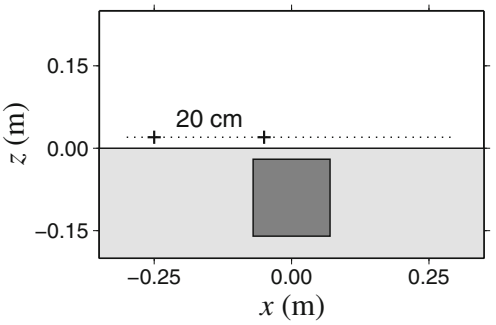

Fig. 11 A vertical section at $y = 0$, of the model in the third example. The dark gray square indicates the graphite cube that is immersed in brine (light gray). The transmitter and receiver pair, distanced 20 cm apart, moved parallel to the x-axis, at $z = 2$ cm

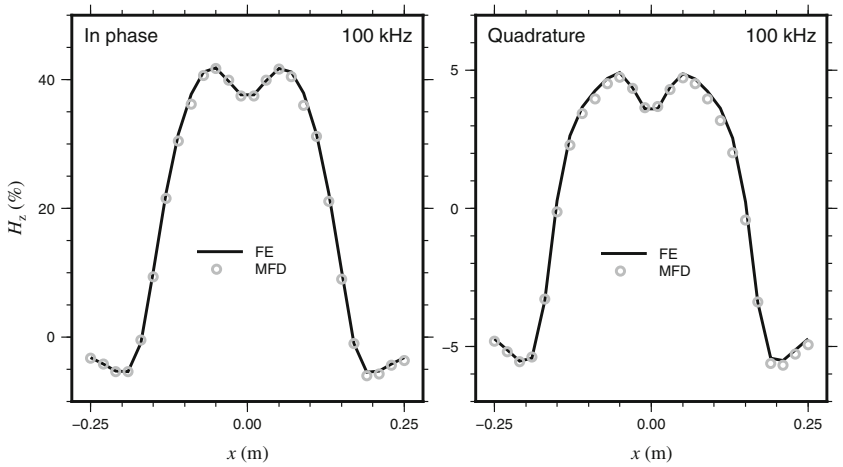

Fig. 12 The in phase and quadrature parts of the z-component of the scattered magnetic field for the frequency of 100 kHz, in the third example. The final MFD results are compared with FE solutions. The MFD solutions correspond to the final grid shown in Fig. 13

solutions for a sufficiently fine tetrahedral grid. Figure 3 also gives reference solutions from the literature [120]. Computation time and memory usage, using MUMPS, for the five iterations are given by Table 1, and vertical sections of the initial and final grids along the two profiles that are parallel to the x and y axes are given in Fig. 5. The good match between the MFD and FE solutions and the reference values, in Figs. 3 and 4, verifies the accuracy of the mimetic finite-difference scheme. The final grid in Fig. 5 shows that the goal-oriented adaptivity mainly concentrates refinement at the observation points and the anomalous region. This is an expected behavior of a goal-oriented adaptivity scheme and shows the reliability of the error estimator proposed in Section 3.1.

4.2 Example 2

The second example represents a land CSEM survey where the EM source is a straight grounded wire that operates at a low frequency (see Fig. 6). The model comprises an anomalous block that is located inside a halfspace. The dimensions of the block in the x-, y- and z-directions are $120 \times 200 \times 400$ m, respectively, and the centre of the top of the block is located at $(1000, 0, -100)$ m. The grounded wire source was 100 m long with end points located at the air-earth interface, at $(0, 0, 0)$ m and $(100, 0, 0)$ m. The conductivities of the anomalous block and the halfspace were 0.2 and 0.02 S/m, respectively, and the frequency was 3 Hz. There was a single observation profile ranging from $(500, 0, 0)$ m to $(1500, 0, 0)$ m, along which the observation points were distanced 20 m apart. The dimensions of the entire domain were $40 \times 40 \times 40$ km and the initial mesh consisted of 10887 tetrahedra. The 100 m wire source was represented as 20 segments of 5 m wires, i.e., $n = 20$ in Eq. 4. For this example, we used six iterations which resulted in a grid with 415768 elements.

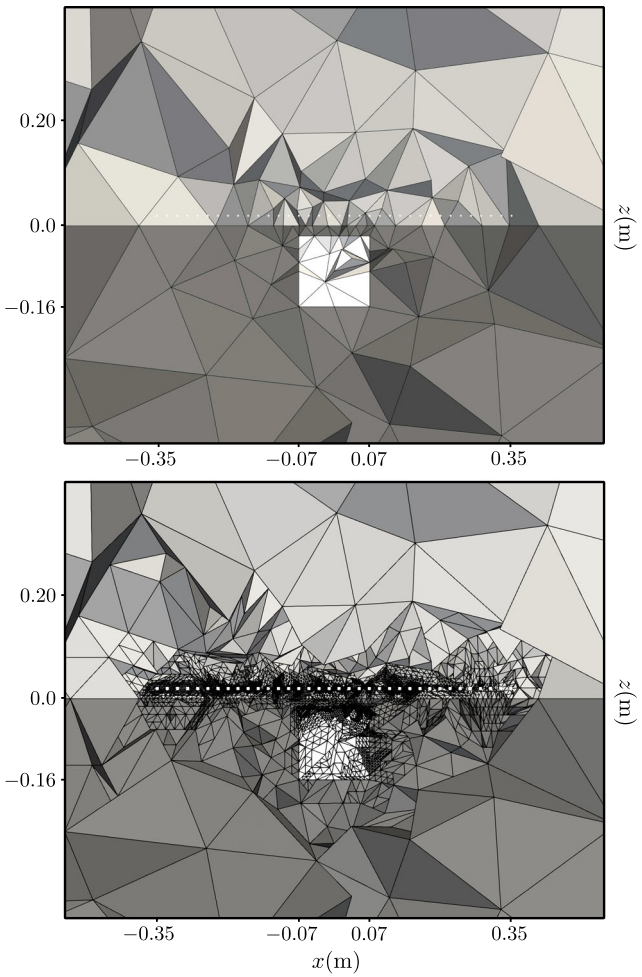

Fig. 13 Close-ups of the sections of the initial (top) and final (bottom) grids through the transmitter-receiver profile, along the x-axis, for goal-oriented mesh adaptivity in the third example. Light and dark gray show the air and brine regions and white shows the graphite cube. The white dots show the transmitter and receiver locations. The final grid corresponds to the MFD data given in Fig. 12

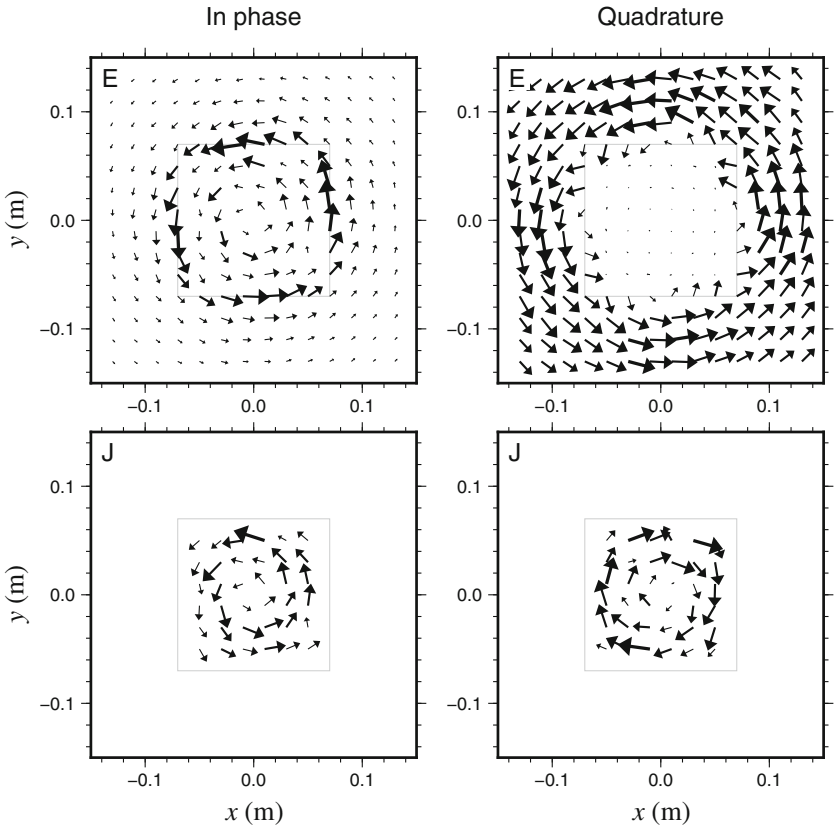

Fig. 14 The total electric field (top) and current density (bottom) for the third example, at a horizontal section at $z = -3$ cm. The light gray rectangle shows the limits of the graphite cube. The sizes of the arrows are normalized by the largest arrow size in each panel. In the bottom panels, the arrows inside the brine region are too small to be visualized

The in phase and quadrature parts of the x-component of the total and scattered electric field at the observation points are depicted in Figs. 7 and 8. Both figures show solutions with the adaptive MFD scheme and FE solutions for a fine tetrahedral grid. The scattered field in Fig. 8 is defined as the total field for the homogeneous halfspace subtracted from the total field due to the halfspace with the anomalous region. Vertical sections of the initial and final grids along the wire source and the profile are given in Fig. 9. The good match between the MFD results and the FE solutions, in Figs. 7 and 8, confirms the accuracy of the mimetic scheme. The final grid in Fig. 9 shows that the mesh adaptivity concentrates refinement mainly at the observation points and the source location. More specifically, the highest amounts of refinement occur at the end points of the wire source, where the electric current is injected into the ground, and those observation points that are closer to the wire source.

For this second example, Fig. 10 gives vector representations of the horizontal component of the electric field and current density at a horizontal section that passes through the anomalous region at the depth of -200 m. For better visualization, in each panel the sizes of the arrows are normalized by the largest arrow size in that panel. These results demonstrate the continuity of the normal component of the current density and the tangential electric field, and the discontinuity of the normal component of the electric field and tangential current density. This verifies the accuracy of the MFD solution across the facets shared by polyhedral elements that belong to different refinement levels (see Section 3.2).

4.3 Example 3

The parameters in the third example are derived from a model that was used for physical scale modelling (PSM) measurements in [36]. This example typifies an airborne EM survey where a magnetic dipole transmitter-receiver pair moves over a highly conductive anomalous region that is located inside a resistive background. We compare the results of the adaptive MFD method with FE solutions. The model comprised a small graphite cube with side lengths of 14 cm that was immersed in brine such that its top was 2 cm below the brine surface (see Fig. 11). The transmitter and receiver were horizontal coplanar loops of wire that moved in the x-direction, at z=2 cm. The transmitter-receiver pair separation was 20 cm and the observations were attributed to the midpoint of the segment connecting the transmitter and receiver. The conductivities of the graphite and brine were 63000 and 7.3 S/m, respectively. We simulated the PSM measurements for the frequency of 100 kHz using 26 vertical magnetic dipole transmitter-receiver pairs. The

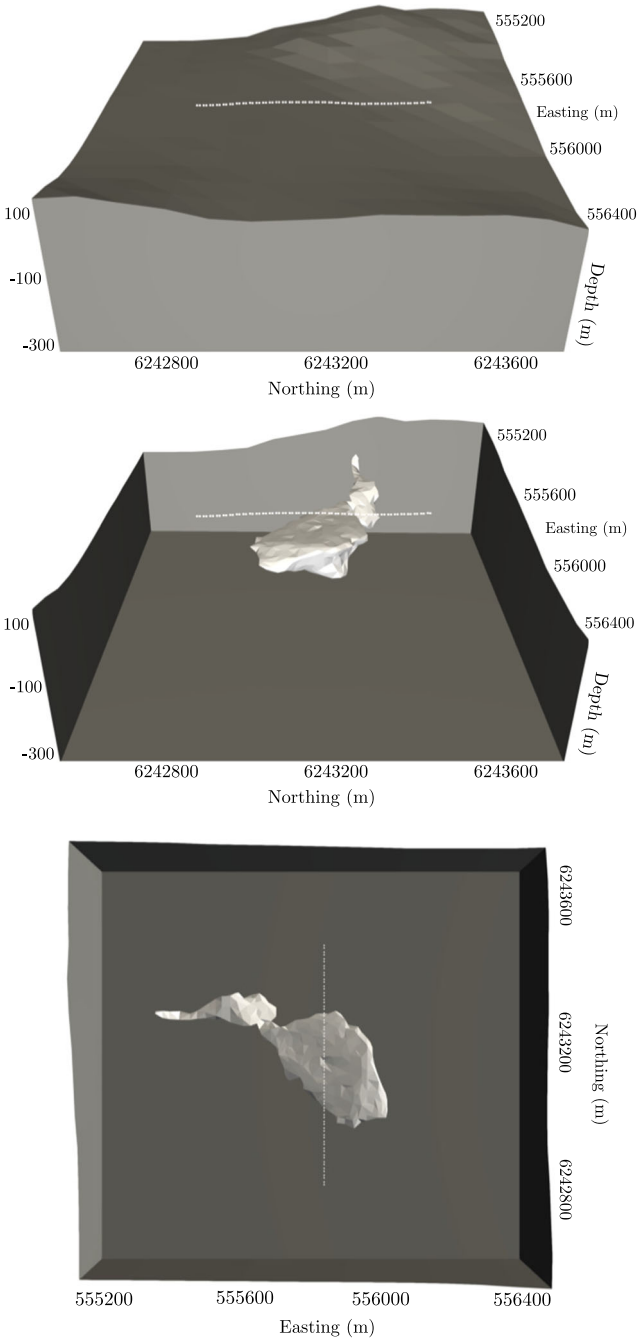

Fig. 15 The realistic model used in the fourth example. Top figure shows the topography of the region. The topography is removed in the middle and bottom figures and the (white) sulphide body is revealed. The white dots show the transmitter and receiver locations. In UTM coordinates, the midpoints of the transmitter-receiver pairs have easting of 555837 m and northing that ranges from 6242800 to 6243500 m

midpoints of these pairs located on the xz plane at z=2 cm and ranging from x=−25 cm to 25 cm. The dimensions of the entire domain were 40 × 40 × 40 m, and the initial mesh consisted of 5327 tetrahedra. In this example, the scattered magnetic field was defined as the total field minus the free-space field, normalized by the free-space field. We represented the vertical magnetic dipoles as horizontal rectangular loops of current with the side length of 2 mm.

While each transmitter in this example demands an individual modelling problem, we generated a single adaptive grid for all the sources. To do this, we modified the definition of the goal-oriented error estimator, given by Eq. 25, to represent the summation of the error estimators for all the sources,

$$\eta_h^g \equiv \sum_{i=1}^{s} \sum_{\mathsf{P}\in\Omega_h} \left(\eta_{h,\mathsf{P},i}\right)^a \left(\eta^w_{h,\mathsf{P},i}\right)^b, \tag{27}$$

where s is the number of sources and $\eta_{h,\mathsf{P},i}$ and $\eta^w_{h,\mathsf{P},i}$ are the error estimators that correspond to the i^{th} primary and adjoint problems, relations (22) and (26), respectively. We note that a single grid for all the sources is naturally larger than each grid that would have been generated for each transmitter. However, this approach greatly improves the efficiency of the mesh adaptivity since at each iteration of the AMR procedure, the direct solver only requires two factorizations of the coefficient matrix in Eq. 22, for the main conductivity model and for the free-space model.

For this third example, we used the error estimator defined by Eq. 27 and six AMR iterations which resulted in a grid with 424340 elements. The in phase and quadrature parts of the z-component of the scattered magnetic field for the adaptive MFD method and FE solutions are given in Fig. 12. Vertical sections of the initial and final grids along the transmitter-receiver profile are given in Fig. 13. The good match between the MFD results and the FE solutions, in Fig. 12, confirms the accuracy and effectiveness of the adaptive mimetic scheme. The final grid in Fig. 13 shows that the mesh adaptivity concentrates refinement at the transmitter and receiver locations, and at the top of the anomalous region. Figure 14 gives vector representations of the horizontal component of the electric field and current density at a horizontal section that passes through the anomalous region at the depth of −3 cm. For these results, a single magnetic dipole was located at (0, 0, 2) cm. As for the previous example, the sizes of the arrows are normalized by the largest arrow size in each panel. The results for the current density show that virtually all the current is confined to the highly conductive graphite cube.

4.4 Example 4

The fourth example represents a real-life complex geological structure with topography (see Fig. 15). This model is based on the Ovoid massive sulfide ore body located at Voisey's Bay, Labrador, Canada. The ore body is composed of 70% massive sulphide and the overburden is

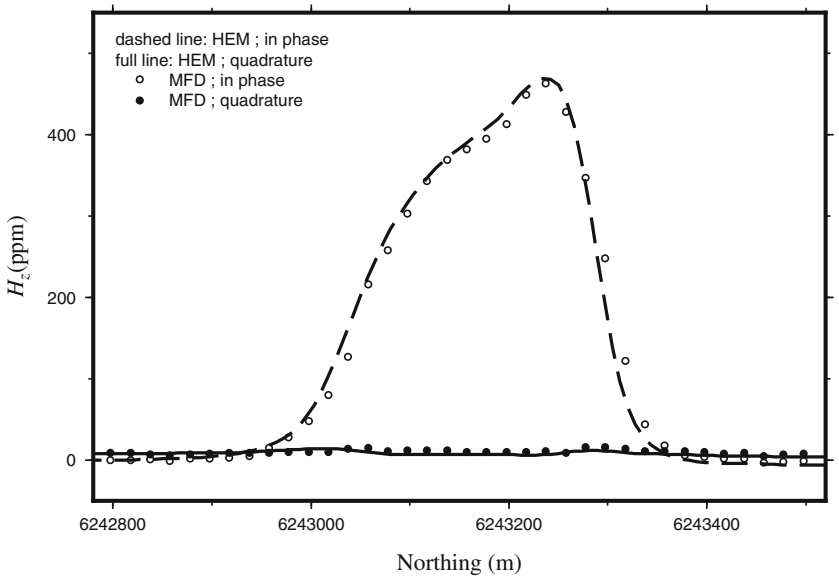

Fig. 16 The final MFD data from the fourth example (circles) compared with the real HEM data (lines). The data are the z-component of the scattered magnetic field which are observed at the receivers and assigned to the middle of the transmitter-receiver pairs. The MFD solutions correspond to the final grid shown in Fig. 17

approximately 20 m [13]. Using the adaptive MFD method presented in this article, a real data set from a HEM survey of the region was simulated [40]. In the HEM survey, the transmitter and receiver were horizontal coplanar coils, distanced 8 m apart, that were towed below the helicopter 30 m above ground. We used 36 transmitter-receiver pairs to simulate data for a single North-South profile, for the frequency of 900 Hz (see Fig. 15). The initial grid consisted of 23070 tetrahedra. The conductivities of the Ovoid and of the background were chosen by trial-and-error in order to match the real data: 0.0005 S/m for the background, 0.01 S/m for the upper roughly 10 m of the Ovoid, and 1000 S/m for its lower part. While the constant conductivities and the sharp boundary used to separate the Ovoid into parts are not realistic, the suitability of this model, demonstrated below, indicates that the overall conductivity of the Ovoid increases with depth.

Using the cumulative error estimator given by Eq. 27, and seven AMR iterations, resulted in a grid with 946727 elements. The in phase and quadrature parts of the z-component of the scattered magnetic field for the adaptive MFD method and the real HEM data, expressed in ppm, are given in Fig. 16. Computation time and memory usage, using MUMPS, for the seven iterations are given by Table 2, and vertical sections of the initial and final grids along the transmitter-receiver profile are given in Fig. 17. The good match between the MFD results and the real data in Fig. 16 verifies the practicality of the presented adaptive mimetic approach in the presence of complex geometry in the computational domain.

4.5 Example 5

The fifth example was used to further evaluate the AMR approach presented in Sections 2 and 3, by comparison with a conventional mesh regeneration technique based on TetGen and a standard edge-based FE scheme (see the introduction for a description and references). The model comprises an x-directed electric dipole on a homogeneous halfspace. The electric dipole was located at the centre of the coordinate system and the observation data were the x-component of the electric field along a y-directed profile from (0, 100, 0) m to (0, 1100, 0) m. In this example, the numerical solutions were compared with analytical values

Table 2 Computation time and memory usage, using MUMPS, and the number of elements, for the seven iterations of the adaptive MFD scheme in the fourth (Ovoid) example

Iteration no.	0	1	2	3	4	5	6	7
No. of elements	23070	39219	66673	113349	192694	327584	556897	946727
Time (s)	0.5	1	2.5	5	9	15	27	50
Memory (MB)	116	240	508	818	1611	2938	5282	9767

Iteration 0 refers to the initial model

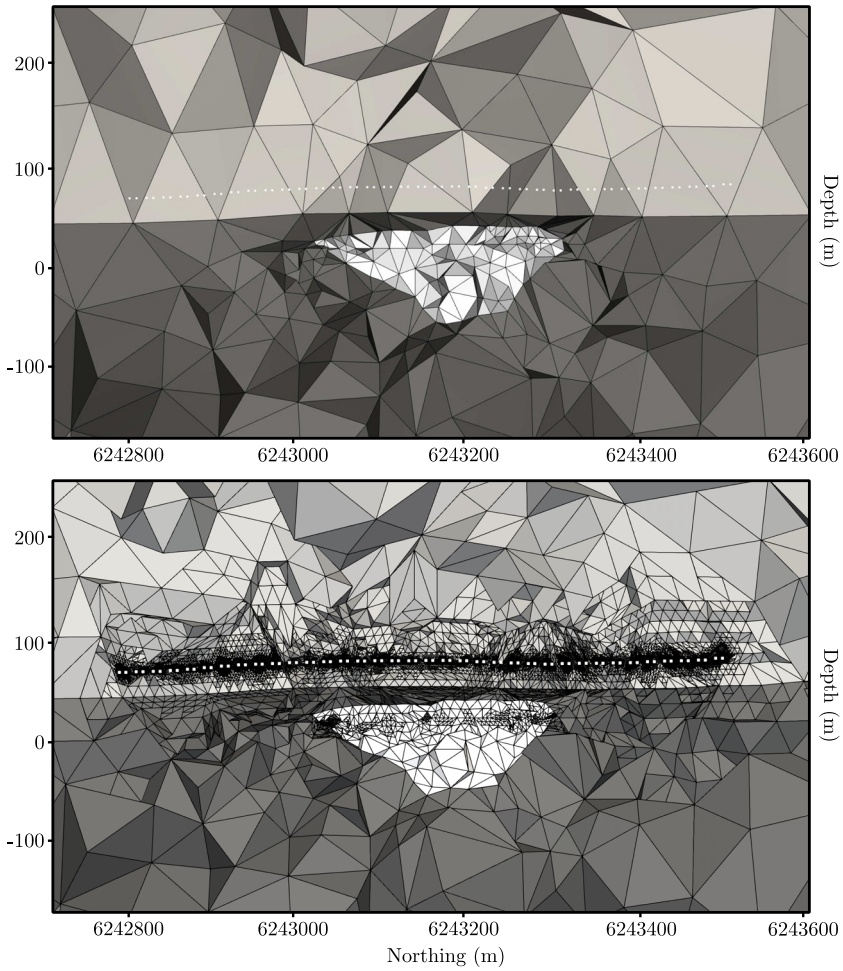

Fig. 17 Close-ups of the sections of the initial (top) and final (bottom) grids through the transmitter-receiver profile, along the northing direction, for goal-oriented mesh adaptivity in the fourth example. Light and dark gray show the air and ground regions and white shows the Ovoid. The white dots show the transmitter and receiver locations. The final grid corresponds to the MFD data given in Fig. 16

for an infinitesimal electric dipole [116]. The initial grid consisted of 17739 tetrahedra and the electric dipole was represented by a one metre grounded wire with end points located at $(-0.5, 0, 0)$ m and $(0.5, 0, 0)$ m. We used 21 observation points along the profile, a conductivity of 0.01 S/m for the halfspace and a frequency of 500 Hz.

Table 3 Computation time and memory usage, using MUMPS, and the number of elements, in the fifth (electric dipole) example

Adaptive method	Iteration no.	0	1	2	3	4	5	6
MFD	No. of elements	17739	25985	55721	81593	119463	174917	211674
Reg. ref.	Time (s)	0.5	1	2.5	4	7	9.5	12
1-irreg.	Memory (MB)	86	149	395	646	1047	1534	1853
MFD	No. of elements	17739	25985	55721	81586	119456	174903	211639
Reg. ref.	Time (s)	0.5	1	2	3.5	8.5	11.5	12
2-irreg.	Memory (MB)	86	145	399	634	968	1500	1841
FE	No. of elements	17739	28764	54089	77205	125581	170278	217054
Mesh regen.	Time (s)	0.5	1	2	3.5	8	11	26
(TetGen)	Memory (MB)	86	179	408	696	1275	1895	2702

The resource usage is given for the six iterations of the adaptive MFD regular refinement (Reg. ref.) method, and the mesh regeneration (Mesh regen.) technique using the FE method. For the MFD method, both 1- and 2-irregularity (irreg.) are considered. Iteration 0 refers to the initial model

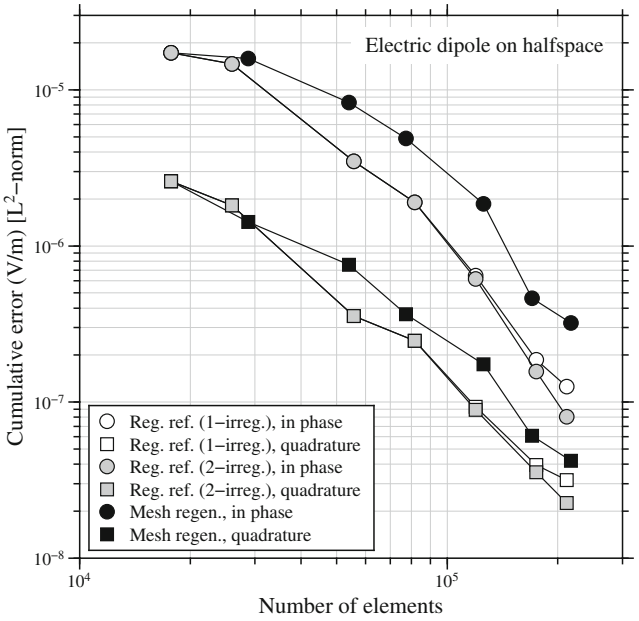

Fig. 18 The L^2-norm of the error at the observation points versus the number of elements in the fifth example. The white, gray and black symbols correspond to the various iterations of the regular refinement (Reg. ref.) approach with 1- and 2-irregularity (irreg.), with the MFD scheme, and the mesh regeneration (Mesh regen.) method, with an FE scheme, respectively

For both the MFD regular refinement approach and the FE mesh regeneration method, we used the error estimator presented in Section 3.1, and the marking strategy described in Section 3.2. At each mesh regeneration step, refinement was performed by designating maximum volumes for the marked elements. Following [87], we chose half of the volume of the marked elements as the maximum volume. Also, we regenerated the grids with the same radius-edge ratio [94] as used to generate the initial grid (this ratio was 1.12). For the MFD scheme, we used both 1- and 2-irregularity and we used six iterations for both the MFD scheme and the mesh regeneration method. Computation time and memory usage, using MUMPS, and the numbers of elements for these six iterations are given by Table 3. The L^2-norm of the error at the observation locations versus the number of elements, for these two methods and for all the iterations, are given in Fig. 18, and vertical sections of the final grids with the MFD scheme, with 2-irregularity, and the mesh regeneration method, along the observation profile, are given in Fig. 19.

We can see, in Fig. 18, that all methods show similar trends of accuracy, but the regular refinement approach consistently shows lower error norm values. If we compare the final grids given by Fig. 19, we can see that the final grid with the MFD scheme shows higher refinement at the source and observation points and less refinement at the regions farther from the source and receiver locations. This higher concentration of refinement at the source and receiver locations with the MFD scheme could explain the higher accuracy achieved by this method in Fig. 18. Moreover, Table 3 shows that, using the sparse direct solver MUMPS, the adaptive MFD scheme with regular refinement is more efficient than the mesh regeneration approach in terms of both computation time and memory usage. In Fig. 18, we also see that the error norms with 2-irregularity are slightly lower than those with 1-irregularity, in the last iterations of the adaptive refinements. The reason is that during the initial iterations of an adaptive regular refinement, typically, all the newly marked elements are only neighbor to elements with the same levels of refinement, and therefore, the subdivision of these marked elements creates, primarily, 1-irregularity. However, at the final iterations, there is a higher likelihood of marking elements whose subdivision would create 2-irregularity. This higher level of non-conformity can help to avoid unnecessary refinements and to use the refinements, instead, in regions with higher impact on the solution accuracy.

5 Conclusions

In this study, we explored the application of the mimetic finite-difference method in conjunction with an adaptive mesh refinement, for the forward modelling of geophysical electromagnetic data. We employed the generality of the mimetic method and implemented an edge-based polyhedral scheme with two levels of non-conformity. We used this octree-like method within an automatic adaptive *h*-refinement procedure where unstructured tetrahedral grids were used as the initial grids and a residual- and jump-based goal-oriented error estimator was employed to mark the elements for refinement, at each iteration. In this method, each marked element is subdivided into eight new tetrahedra by regular refinement, which potentially adds new nodes to the neighboring elements. Since the mimetic finite-difference method naturally supports polyhedra, these additional nodes do note create hanging nodes, and so, any modification of the numerical scheme is avoided.

We validated the accuracy of the mimetic scheme and the effectiveness of the proposed adaptivity procedure using benchmark and realistic models that represented various magnetotelluric and controlled-source survey scenarios. We started with a coarse tetrahedral grid and used several iterations to reach a desired accuracy. The goal-oriented

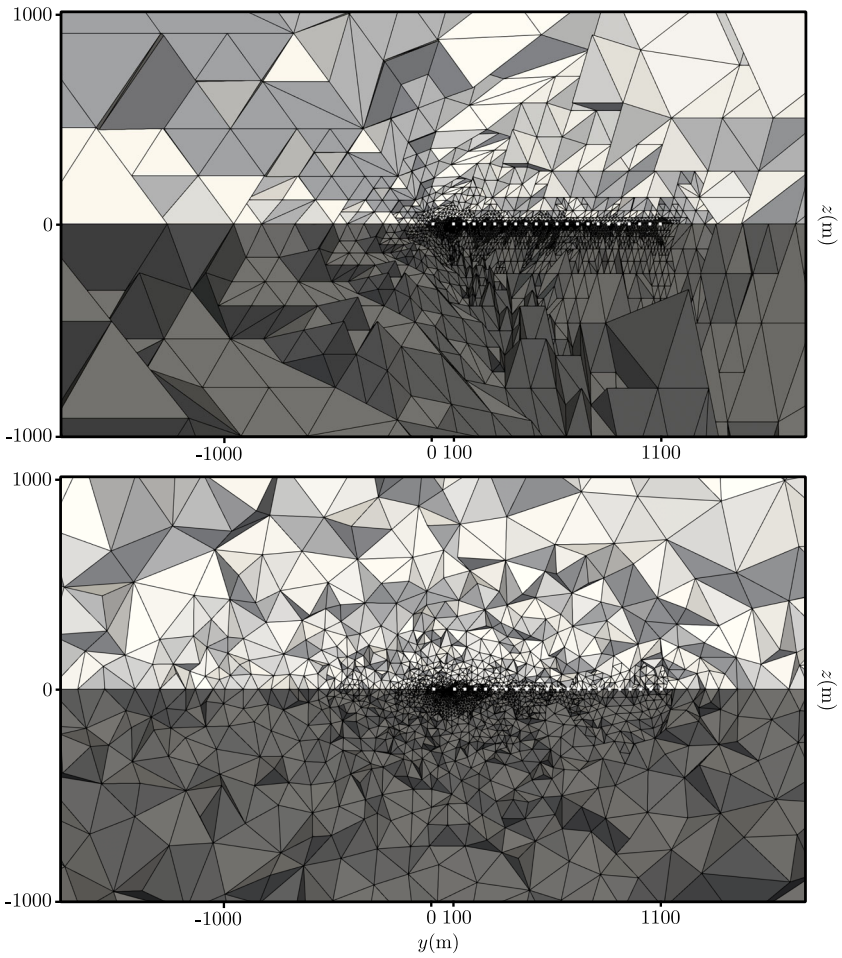

Fig. 19 Vertical sections of the final grids with the MFD scheme, with 2-irregularity (top), and the mesh regeneration method (bottom), along the observation profile, for goal-oriented mesh adaptivity in the fifth example. Light and dark gray show the air and ground regions and the white dots show the source and receiver locations. Note that the electric dipole source is x-directed. These grids correspond to the error norm values reported for the last iterations of the corresponding graphs in Fig. 18

method, generally, concentrated the refinements at the source and observation locations and at the interfaces of the materials with contrasting conductivities. The results showed good agreements between the adaptive mimetic finite-difference solutions and the numerical and real reference data. Using a benchmark model with analytical solutions, we also compared the proposed adaptive method with a conventional mesh regeneration approach where the adaptive mimetic scheme, with regular refinement, reached a higher accuracy, with similar numbers of elements. Also, for similar numbers of elements, the adaptive mimetic approach was found to be more efficient than the mesh regeneration technique, in terms of computation time and memory usage. Using the same example, a comparison was made between the adaptive mimetic scheme with 1- and 2-irregularity where 2-irregularity gained a higher accuracy, with similar numbers of elements.

The successful results of this study suggest that the mimetic finite-difference method can be considered as a more flexible alternative to the standard finite-element or finite-volume methods, for the modelling of geophysical electromagnetic data. In our future works, we will consider alternative formulations of the geophysical electromagnetic modelling problem and we will explore the extension of the proposed adaptive refinement approach to the electromagnetic inverse problem.

Acknowledgements We acknowledge the support of Research & Development Corporation Newfoundland and Labrador (RDC), Natural Sciences and Engineering Research Council of Canada (NSERC), and the Canada Research Chairs program (CRC).

References

1. Aarnes, J.E., Krogstad, S., Lie, K.A.: Multiscale mixed/mimetic methods on corner-point grids. Comput. Geosci. **12**(3), 297–315 (2008)
2. Ainsworth, M., Demkowicz, L., Kim, C.W.: Analysis of the equilibrated residual method for a posteriori error estimation on meshes with hanging nodes. Comput. Methods Appl. Mech. Eng. **196**(37-40), 3493–3507 (2007)
3. Ainsworth, M., Oden, J.T.: A Posteriori Error Estimation in Finite Element Analysis. John Wiley & Sons, New York (2011)

4. Ainsworth, M., Senior, B.: Aspects of an adaptive hp-finite element method:Adaptive strategy, conforming approximation and efficient solvers. Comput. Methods Appl. Mech. Eng. **150**(1-4), 65–87 (1997)
5. Amestoy, P.R., Guermouche, A., L'Excellent, J.Y., Pralet, S.: Hybrid scheduling for the parallel solution of linear systems. Parallel Comput. **32**, 136–156 (2006)
6. Antonietti, P.F., da Veiga, L.B., Lovadina, C., Verani, M.: Hierarchical a posteriori error estimators for the mimetic discretization of elliptic problems. SIAM J. Numer. Anal. **51**(1), 654–675 (2013)
7. Arnold, D.N., Bochev, P.B., Lehoucq, R.B., Nicolaides, R.A., Shashkov, M.: Compatible Spatial Discretizations, vol. 142. Springer Science & Business Media, New York (2007)
8. Aulisa, E., Calandrini, S., Capodaglio, G.: An improved multigrid algorithm for n-irregular meshes with subspace correction smoother. Comput. Math. Appl. **76**(3), 620–632 (2018)
9. Aulisa, E., Capodaglio, G., Ke, G.: Construction of h-refined continuous finite element spaces with arbitrary hanging node configurations and applications to multigrid algorithms. SIAM J. Sci. Comput. **41**(1), A480–A507 (2019)
10. Avdeev, D., Avdeeva, A.: 3D Magnetotelluric inversion using a limited-memory quasi-newton optimization. Geophysics **74**, F45–F57 (2009)
11. Avdeeva, A., Moorkamp, M., Avdeev, D., Jegen, M., Miensopust, M.: Three-dimensional inversion of magnetotelluric impedance tensor data and full distortion matrix. Geophys. J. Int. **202**, 464–481 (2015)
12. Baitsch, M., Hartmann, D.: Piecewise polynomial shape functions for hp-finite element methods. Comput. Methods Appl. Mech. Eng. **198**(13-14), 1126–1137 (2009)
13. Balch, S.J.: Geophysics in mineral exploration: fundamentals and case histories. Ni-Cu Sulphide deposits with examples from Voisey's Bay. In: Practical Geophysics III Northwest Mining Association (2000)
14. Beck, R., Hiptmair, R., Hoppe, R.H., Wohlmuth, B.: Residual based a posteriori error estimators for eddy current computation. ESAIM Math. Model. Numer. Anal. **34**(1), 159–182 (2000)
15. Becker, R., Rannacher, R.: An optimal control approach to a posteriori error estimation in finite element methods. Acta Numerica **10**, 1–102 (2001)
16. Brenner, S.C., Scott, L.R.: The Mathematical Theory of Finite Element Methods. Springer, New York (2008)
17. Brezzi, F., Buffa, A.: Innovative mimetic discretizations for electromagnetic problems. J. Comput. Appl. Math. **234**(6), 1980–1987 (2010)
18. Brezzi, F., Lipnikov, K., Shashkov, M.: Convergence of the mimetic finite difference method for diffusion problems on polyhedral meshes. SIAM J. Numer. Anal. **43**(5), 1872–1896 (2005)
19. Brezzi, F., Lipnikov, K., Shashkov, M.: Convergence of mimetic finite difference method for diffusion problems on polyhedral meshes with curved faces. Math. Model. Methods Appl. Sci. **16**(02), 275–297 (2006)
20. Brezzi, F., Lipnikov, K., Shashkov, M., Simoncini, V.: A new discretization methodology for diffusion problems on generalized polyhedral meshes. Comput. Methods Appl. Mech. Eng. **196**(37-40), 3682–3692 (2007)
21. Brezzi, F., Lipnikov, K., Simoncini, V.: A family of mimetic finite difference methods on polygonal and polyhedral meshes. Math. Model. Methods Appl. Sci. **15**(10), 1533–1551 (2005)
22. Brezzi, F., Marini, L.D.: Virtual element methods for plate bending problems. Comput. Methods Appl. Mech. Eng. **253**, 455–462 (2013)
23. Cangiani, A., Manzini, G.: Flux reconstruction and solution post-processing in mimetic finite difference methods. Comput. Methods Appl. Mech. Eng. **197**(9-12), 933–945 (2008)
24. Cangiani, A., Manzini, G., Russo, A.: Convergence analysis of the mimetic finite difference method for elliptic problems. SIAM J. Numer. Anal. **47**(4), 2612–2637 (2009)
25. Cho, Y.S., Jun, S., Im, S., Kim, H.G.: An improved interface element with variable nodes for non-matching finite element meshes. Comput. Methods Appl. Mech. Eng. **194**(27-29), 3022–3046 (2005)
26. Commer, M., Newman, G.A.: Three-dimensional controlled-source electromagnetic and magnetotelluric joint inversion. Geophys. J. Int. **178**, 1305–1316 (2009)
27. Da Veiga, L.B., Brezzi, F., Marini, L.D.: Virtual elements for linear elasticity problems. SIAM J. Numer. Anal. **51**(2), 794–812 (2013)
28. Da Veiga, L.B., Gyrya, V., Lipnikov, K., Manzini, G.: Mimetic finite difference method for the Stokes problem on polygonal meshes. J. Comput. Phys. **228**(19), 7215–7232 (2009)
29. Da Veiga, L.B., Lipnikov, K.: A mimetic discretization of the Stokes problem with selected edge bubbles. SIAM J. Sci. Comput. **32**(2), 875–893 (2010)
30. Davis, K., Li, Y.: Fast solution of geophysical inversion using adaptive mesh, space-filling curves and wavelet compression. Geophys. J. Int. **185**(1), 157–166 (2011)
31. Davis, K., Li, Y.: Efficient 3D inversion of magnetic data via octree-mesh discretization, space-filling curves, and wavelets. Geophysics **78**(5), J61–J73 (2013)
32. Demkowicz, L.: Computing with Hp-Adaptive Finite Elements: Volume I One and Two Dimensional Elliptic and Maxwell Problems. Chapman and Hall/CRC, London (2006)
33. Demkowicz, L., Kurtz, J., Pardo, D., Paszynski, M., Rachowicz, W., Zdunek, A.: Computing with Hp-Adaptive Finite Elements: Volume II, Frontiers: Three-dimensional Elliptic and Maxwell Problems with Applications. Applied Mathematics and Nonlinear Science. Chapman and Hall/CRC, London (2008)
34. Droniou, J., Eymard, R., Gallouët, T., Herbin, R.: A unified approach to mimetic finite difference, hybrid finite volume and mixed finite volume methods. Math. Model. Methods Appl. Sci. **20**(02), 265–295 (2010)
35. Farquharson, C.G., Craven, J.A.: Three-dimensional inversion of Magnetotelluric data for mineral exploration: An example from the McArthur River uranium deposit, Saskatchewan, Canada. J. Appl. Geophys. **68**, 450–458 (2008)
36. Farquharson, C.G., Duckworth, K., Oldenburg, D.W.: Comparison of integral equation and physical scale modeling of the electromagnetic responses of models with large conductivity contrasts. Geophysics **71**, G169–G177 (2006)
37. Farquharson, C.G., Miensopust, M.P.: Three-dimensional finite-element modelling of magnetotelluric data with a divergence correction. J. Appl. Geophys. **75**, 699–710 (2011)
38. Franke-Börner, A.: Three-dimensional finite element simulation of magnetotelluric fields on unstructured grids. Ph.D. thesis, TU Bergakademie Freiberg (2013)
39. Fries, T.P., Byfut, A., Alizada, A., Cheng, K.W., Schröder, A.: Hanging nodes and XFEM. Int. J. Numer. Methods Eng. **86**(4-5), 404–430 (2011)
40. Garrie, D.G.: Dighem survey for diamond fields resources Inc. Archean resources Ltd. Voisey's Bay, Labrador Survey Report 1202 Dighem, A division of CGG Canada Ltd (1995)
41. Grayver, A.: Parallel three-dimensional magnetotelluric inversion using adaptive finite-element method. Part I: theory and synthetic study. Geophys. J. Int. **202**, 584–603 (2015)

42. Grayver, A.V., Kolev, T.V.: Large-scale 3D geoelectromagnetic modeling using parallel adaptive high-order finite element method. Geophysics **80**(6), E277–E291 (2015)
43. Gupta, A.K.: A finite element for transition from a fine to a coarse grid. Int. J. Numer. Methods Eng. **12**(1), 35–45 (1978)
44. Gyrya, V., Lipnikov, K.: High-order mimetic finite difference method for diffusion problems on polygonal meshes. J. Comput. Phys. **227**(20), 8841–8854 (2008)
45. Gyrya, V., Lipnikov, K.: The arbitrary order mimetic finite difference method for a diffusion equation with a non-symmetric diffusion tensor. J. Comput. Phys. **348**, 549–566 (2017)
46. Gyrya, V., Lipnikov, K., Manzini, G., Svyatskiy, D.: M-adaptation in the mimetic finite difference method. Math. Model. Methods Appl. Sci. **24**(08), 1621–1663 (2014)
47. Haber, E., Ascher, U.M., Aruliah, D.A., Oldenburg, D.W.: Fast simulation of 3D electromagnetic problems using potentials. J. Comput. Phys. **163**, 150–171 (2000)
48. Haber, E., Heldmann, S.: An octree multigrid method for quasi-static Maxwell's equations with highly discontinuous coefficients. J. Comput. Phys. **223**, 783–796 (2007)
49. Haber, E., Ruthotto, L.: A multiscale finite volume method for Maxwell's equations at low frequencies. Geophys. J. Int. **199**(2), 1268–1277 (2014)
50. Haber, E., Schwarzbach, C.: Parallel inversion of large-scale airborne time-domain electromagnetic data with multiple OcTree meshes. Inverse Probl. **30**(5), 055011 (2014)
51. Han, N., Nam, M.J., Kim, H.J., Lee, T.J., Song, Y., Suh, J.H.: Efficient three-dimensional inversion of Magnetotelluric data using approximate sensitivities. Geophys. J. Int. **175**, 477–485 (2008)
52. Horesh, L., Haber, E.: A second order discretization of Maxwell's equations in the Quasi-static regime on OcTree grids. SIAM J. Sci. Comput. **33**, 2805–2822 (2011)
53. Hyman, J., Shashkov, M., Steinberg, S.: The numerical solution of diffusion problems in strongly heterogeneous non-isotropic materials. J. Comput. Phys. **132**(1), 130–148 (1997)
54. Hyman, J.M., Shashkov, M.: Approximation of boundary conditions for mimetic finite-difference methods. Comput. Math. Appl. **36**(5), 79–99 (1998)
55. Jahandari, H., Ansari, S., Farquharson, C.G.: Comparison between staggered grid finite-volume and edge-based finite-element modelling of geophysical electromagnetic data on unstructured grids. J. Appl. Geophys. **138**, 185–197 (2017)
56. Jahandari, H., Farquharson, C.G.: 3-D minimum-structure inversion of magnetotelluric data using the finite-element method and tetrahedral grids. Geophys. J. Int. **211**, 1189–1205 (2017)
57. Key, K., Ovall, J.: A parallel goal-oriented adaptive finite element method for 2.5-D electromagnetic modelling. Geophys. J. Int. **186**, 137–154 (2011)
58. Key, K., Weiss, C.: Adaptive finite-element modeling using unstructured grids: The 2D magnetotelluric example. Geophysics **71**, G291–G299 (2006)
59. Kordy, M., Wannamaker, P., Maris, V., Cherkaev, E., Hill, G.: 3-D magnetotelluric inversion including topography using deformed hexahedral edge finite elements and direct solvers parallelized on SMP computers - Part I: forward problem and parameter jacobians. Geophys. J. Int. **204**, 74–93 (2016)
60. Kruglyakov, M., Geraskin, A., Kuvshinov, A.: Novel accurate and scalable 3-D MT forward solver based on a contracting integral equation method. Comput. Geosci. **96**, 208–217 (2016)
61. Li, Y., Key, K.: 2D marine controlled-source electromagnetic modeling: Part 1 - An adaptive finite element algorithm. Geophysics **72**(2), WA51–WA62 (2007)
62. Li, Y., Pek, J.: Adaptive finite element modelling of two-dimensional magnetotelluric fields in general anisotropic media. Geophys. J. Int. **175**(3), 942–954 (2008)
63. Lipnikov, K., Manzini, G.: Discretization of mixed formulations of elliptic problems on polyhedral meshes. In: Building Bridges: Connections and Challenges in Modern Approaches to Numerical Partial Differential Equations, pp. 311–342. Springer (2016)
64. Lipnikov, K., Manzini, G., Brezzi, F., Buffa, A.: The mimetic finite difference method for the 3D magnetostatic field problems on polyhedral meshes. J. Comput. Phys. **230**(2), 305–328 (2011)
65. Lipnikov, K., Manzini, G., Shashkov, M.: Mimetic finite difference method. J. Comput. Phys. **257**, 1163–1227 (2014)
66. Lipnikov, K., Morel, J., Shashkov, M.: Mimetic finite difference methods for diffusion equations on non-orthogonal non-conformal meshes. J. Comput. Phys. **199**(2), 589–597 (2004)
67. Lipnikov, K., Moulton, J.D., Svyatskiy, D.: A multilevel multiscale mimetic $\left(\mathrm{M}^3\right)$ method for two-phase flows in porous media. J. Comput. Phys. **227**(14), 6727–6753 (2008)
68. Lipnikov, K., Shashkov, M., Svyatskiy, D.: The mimetic finite difference discretization of diffusion problem on unstructured polyhedral meshes. J. Comput. Phys. **211**(2), 473–491 (2006)
69. Liska, R., Shashkov, M., Ganzha, V.: Analysis and optimization of inner products for mimetic finite difference methods on a triangular grid. Math. Comput. Simul. **67**(1-2), 55–66 (2004)
70. Liu, W., Farquharson, C.G., Zhou, J., Li, X.: A rational krylov subspace method for 3D modeling of grounded electrical source airborne time-domain electromagnetic data. J. Geophys. Eng. **16**(2), 451–462 (2019)
71. Liu, Y., Xu, Z., Li, Y.: Adaptive finite element modelling of three-dimensional magnetotelluric fields in general anisotropic media. J. Appl. Geophys. **151**, 113–124 (2018)
72. Mackie, R.L., Madden, T.R.: Three-dimensional magnetotelluric inversion using conjugate gradients. Geophys. J. Int. **115**, 215–229 (1993)
73. Mackie, R.L., Madden, T.R., Wannamaker, P.: 3-D magnetotelluric modeling using difference equations - theory and comparisons to integral equation solutions. Geophysics **58**, 215–226 (1993)
74. Madden, T.R., Mackie, R.L.: Three-dimensional magnetotelluric modeling and inversion. Proc. IEEE **77**, 318–333 (1989)
75. Mitsuhata, Y., Uchida, T.: 3D magnetotelluric modeling using the T-Ω finite-element method. Geophysics **69**(1), 108–119 (2004)
76. Mogi, T.: Three-dimensional electromagnetic modeling of magnetotelluric data using finite element method. J. Appl. Geophys. **35**, 185–189 (1996)
77. Morton, D., Tyler, J., Dorroh, J.: A new 3D finite element for adaptive h-refinement in 1-irregular meshes. Int. J. Numer. Methods Eng. **38**(23), 3989–4008 (1995)
78. Nam, M.J., Kim, H.J., Song, Y., Lee, T.J., Son, J.S., Suh, J.H.: 3D magnetotelluric modelling including surface topography. Geophys. Prospect. **55**, 277–287 (2007)
79. Newman, G.A., Alumbaugh, D.L.: Three-dimensional magnetotelluric inversion using non-linear conjugate gradients. Geophys. J. Int. **140**, 410–424 (2000)
80. Oden, J.T., Prudhomme, S.: Goal-oriented error estimation and adaptivity for the finite element method. Comput. Math. Appl. **41**(5-6), 735–756 (2001)
81. Ong, M.E.G.: Uniform refinement of a tetrahedron. SIAM J. Sci. Comput. **15**(5), 1134–1144 (1994)
82. Ovall, J.S.: Asymptotically exact functional error estimators based on superconvergent gradient recovery. Numer. Math. **102**(3), 543–558 (2006)
83. Pardo, D., Demkowicz, L., Torres-Verdin, C., Paszynski, M.: A self-adaptive goal-oriented hp-finite element method with

electromagnetic applications. Part II: electrodynamics. Comput. Methods Appl. Mech. Eng. **196**(37–40), 3585–3597 (2007)
84. Patro, P.K., Uyeshima, M., Siripunvaraporn, W.: Three-dimensional inversion of magnetotelluric phase tensor data. Geophys. J. Int. **192**, 58–66 (2013)
85. Rachowicz, W., Oden, J.T., Demkowicz, L.: Toward a universal hp adaptive finite element strategy part 3. Design of hp meshes. Comput. Methods Appl. Mech. Eng. **77**(1-2), 181–212 (1989)
86. Rannacher, R., Suttmeier, F.T.: A posteriori error control in finite element methods via duality techniques: Application to perfect plasticity. Comput. Mech. **21**(2), 123–133 (1998)
87. Ren, Z., Kalscheuer, T., Greenhalgh, S., Maurer, H.: A goal-oriented adaptive finite-element approach for plane wave 3-D electromagnetic modelling. Geophys. J. Int. **194**, 700–718 (2013)
88. Rizzuti, G.: The optimized virtual element method for the Helmholtz equation: a preliminary study. In: SEG Technical Program Expanded Abstracts 2018, pp. 3898–3902 (2018). Society of Exploration Geophysicists
89. Rodrigo, C., Gaspar, F.J., Hu, X., Zikatanov, L.: A finite element framework for some mimetic finite difference discretizations. Comput. Math. Appl. **70**(11), 2661–2673 (2015)
90. Sasaki, Y.: Three-dimensional inversion of static-shifted magnetotelluric data. Earth Planets Space **56**, 239–248 (2004)
91. Sasaki, Y., Meju, M.A.: Three-dimensional joint inversion for Magnetotelluric resistivity and static shift distributions in complex media. J. Geophys. Res. Solid Earth **111**, B05101 (2006)
92. Schröder, A.: Constrained approximation in hp-fem: Unsymmetric subdivisions and multi-level hanging nodes. In: Spectral and High Order Methods for Partial Differential Equations, pp. 317–325. Springer (2011)
93. Schwarzbach, C., Börner, R.U., Spitzer, K.: Three-dimensional adaptive higher order finite element simulation for geo-electromagnetics–a marine CSEM example. Geophys. J. Int. **187**, 63–74 (2011)
94. Si, H.: TetGen, a quality tetrahedral mesh generator and three-dimensional delaunay triangulator, v1.3. Technical Report 9 Weierstrass Institute for Applied Analysis and Stochastics (2004)
95. Siripunvaraporn, W., Egbert, G., Lenbury, Y.: Numerical accuracy of magnetotelluric modeling: a comparison of finite difference approximations. Earth Planets Space **54**, 721–725 (2002)
96. Siripunvaraporn, W., Egbert, G., Lenbury, Y., Uyeshima, M.: Three-dimensional Magnetotelluric inversion: data-space method. Phys. Earth Planet. Inter. **150**, 3–14 (2005)
97. Siripunvaraporn, W., Sarakorn, W.: An efficient data space conjugate gradient Occam's method for three-dimensional Magnetotelluric inversion. Geophys. J. Int. **186**, 567–579 (2011)
98. Smith, J.T., Booker, J.R.: Rapid inversion of two- and three-dimensional magnetotelluric data. J. Geophys. Res. **96**, 3905–3922 (1991)
99. Šolín, P., Červenỳ, J., Doležel, I.: Arbitrary-level hanging nodes and automatic adaptivity in the hp-FEM. Math. Comput. Simul. **77**(1), 117–132 (2008)
100. Šolın, P., Demkowicz, L.: Goal-oriented hp-adaptivity for elliptic problems. Comput. Methods Appl. Mech. Eng. **193**(6-8), 449–468 (2004)
101. Subramanian, V., Perot, J.B.: Higher-order mimetic methods for unstructured meshes. J. Comput. Phys. **219**(1), 68–85 (2006)
102. Tietze, K., Ritter, O., Egbert, G.D.: 3-D joint inversion of the magnetotelluric phase tensor and vertical magnetic transfer functions. Geophys. J. Int. **203**, 1128–1148 (2015)
103. Ting, S.C., Hohmann, G.W.: Integral equation modeling of three-dimensional magnetotelluric response. Geophysics **46**, 182–197 (1981)
104. Trapp, K.A.: Inner products in covolume and mimetic methods. ESAIM Math. Model. Numer. Anal. **42**(6), 941–959 (2008)
105. Beirão da Veiga, L., Brezzi, F., Cangiani, A., Manzini, G., Marini, L.D., Russo, A.: Basic principles of virtual element methods. Math. Model. Methods Appl. Sci. **23**(01), 199–214 (2013)
106. Beirão da Veiga, L., Manzini, G.: An a posteriori error estimator for the mimetic finite difference approximation of elliptic problems. Int. J. Numer. Methods Eng. **76**(11), 1696–1723 (2008)
107. da Veiga, L.B.: A residual based error estimator for the mimetic finite difference method. Numer. Math. **108**(3), 387–406 (2008)
108. da Veiga, L.B.: A mimetic finite difference method for linear elasticity. M2AN Math. Model. Numer. Anal **44**(2), 231–250 (2010)
109. da Veiga, L.B., Droniou, J., Manzini, G.: A unified approach to handle convection terms in mixed and hybrid finite volumes and mimetic finite difference methods. IMA J. Numer. Anal. **31**(4), 1357–1401 (2010)
110. da Veiga, L.B., Lipnikov, K., Manzini, G.: Convergence of the mimetic finite difference method for the Stokes problem on polyhedral meshes. SIAM J. Numer. Anal **48**(4), 1419–1443 (2010)
111. da Veiga, L.B., Lipnikov, K., Manzini, G.: The Mimetic Finite Difference Method for Elliptic Problems, vol. 11. Springer, New York (2014)
112. da Veiga, L.B., Manzini, G.: A higher-order formulation of the mimetic finite difference method. SIAM J. Sci. Comput. **31**(1), 732–760 (2008)
113. Verfürth, R.: A posteriori error estimation techniques for finite element methods. OUP Oxford. Oxford University Press, Oxford (2013)
114. Vohralík, M., Wohlmuth, B.I.: Mixed finite element methods: implementation with one unknown per element, local flux expressions, positivity, polygonal meshes, and relations to other methods. Math. Model. Methods Appl. Sci. **23**(05), 803–838 (2013)
115. Wannamaker, P.E.: Advances in three-dimensional magnetotelluric modeling using integral equations. Geophysics **56**, 1716–1728 (1991)
116. Ward, S.M., Hohmann, G.W.: Electromagnetic theory for geophysical applications. In: Nabighian, M.N. (ed.) Electromagnetic Methods in Applied Geophysics, Volume 1, Theory, pp. 131–308 (1988). Society of Exploration Geophysicists
117. Xiao, Q., Cai, X., Xu, X., Liang, G., Zhang, B.: Application of the 3D Magnetotelluric inversion code in a geologically complex area. Geophys. Prospect. **58**, 1177–1192 (2010)
118. Zander, N., Bog, T., Kollmannsberger, S., Schillinger, D., Rank, E.: Multi-level hp-adaptivity: high-order mesh adaptivity without the difficulties of constraining hanging nodes. Comput. Mech. **55**(3), 499–517 (2015)
119. Zhang, L., Koyama, T., Utada, H., Yu, P., Wang, J.: A regularized three-dimensional magnetotelluric inversion with a minimum gradient support constraint. Geophys. J. Int. **189**, 296–316 (2012)
120. Zhdanov, M.S., Varentsov, I.M., Weaver, J.T., Golubev, N.G., Krylov, V.A.: Methods for modelling electromagnetic fields: results from COMMEMI - the international project on the comparison of modelling methods for electromagnetic induction. J. Appl. Geophys. **37**, 133–271 (1997)